PAPER

Check for updates

Atmospheric oxidation impact on sea spray produced ice nucleating particles†

Paul J. DeMott, [*a] Thomas C. J. Hill, [a] Kathryn A. Moore, [a] Russell J. Perkins, [a] Liora E. Mael,[bc] Heidi L. Busse,[bd] Hansol Lee, [e] Chathuri P. Kaluarachchi, [e] Kathryn J. Mayer, [bf] Jonathan S. Sauer, [b] Brock A. Mitts,[b] Alexei V. Tivanski, [e] Vicki H. Grassian, [bgh] Christopher D. Cappa, [i] Timothy H. Bertram [j] and Kimberly A. Prather [bg]

The ocean provides a nearly continuous source of certain primary particles emitted as sea spray from bubble bursting that are active as ice nucleating particles. They can impact ice formation, radiative transfer and precipitation processes in regions overlain by supercooled clouds. However, factors affecting their efficacy over time in the marine boundary layer are unresolved. One factor not previously evaluated is the impact of photochemical aging on the ice nucleating ability of emitted particles. We explore this factor for sea spray particles for the first time *via* measurements of aerosols produced in a wave flume during a mesocosm experiment and using an oxidation flow reactor for exposing particles to oxidation by hydroxyl radicals. It is found that any amount of aging (here from 3 to 8 days equivalent) can often lead to degradation in ice nucleating particles concentrations, by factors of 2 to 5 times. By using an aerosol concentrator to enhance collection of ice nucleating particles (INPs) from a continuous flow chamber for offline analyses by transmission electron microscopy, atomic force microscopy, and Raman spectroscopy, compositional and morphological analyses of particles on different days suggested that so-called core−shell type sea salt INPs are particularly sensitive to oxidation. Raman libraries of the compositions of sea spray produced INPs were augmented herein, but a comprehensive understanding of the large range of INP compositions active at different temperatures remains elusive. Losses of particles with diameters above 2 μm in the flow reactor prevented full assessment of oxidation impacts at those sizes, and these losses secondarily confirmed supermicron sea spray as a predominant INP size class. While mechanisms for oxidative losses remain to be resolved, results imply that these reduce the ice nucleating activity of sea spray produced INPs by an equivalent temperature depression of ~2 K during times of solar insolation over oceans.

Environmental significance

Over vast remote regions of the oceanic atmosphere, primary sea spray aerosol (SSA) emissions may provide the major source of ice nucleating particles (INPs) to the atmosphere, providing control over the liquid *versus* ice phase, and, consequently, the radiative properties of extensive, cold stratiform clouds. Since SSA is reactive under exposure to sunlight, oxidative radicals, and other trace gases, there is a need to understand the impact of oxidation on SSA INPs. The action of atmospheric oxidation in reducing the ice nucleation activity of SSA INPs found in the present studies reinforces the centrality of the role of already limited SSA INP emissions on supporting deep cloud supercooling over cold ocean regions, which limits solar radiation reaching the surface there.

aDepartment of Atmospheric Science, Colorado State University, Fort Collins, Colorado 80523, USA. E-mail: Paul.Demott@colostate.edu

bDepartment of Chemistry and Biochemistry, University of California, La Jolla, San Diego, California 92093, USA

cDepartment of Mechanical Engineering, University of Colorado, Boulder, CO, 80309, USA

dDepartment of Chemistry, The Pennsylvania State University, University Park, Pennsylvania 16802, USA

eDepartment of Chemistry, University of Iowa, Iowa City, Iowa 52242, USA

fDepartment of Chemistry, Colorado State University, Fort Collins, Colorado 80523, USA

gScripps Institution of Oceanography, University of California, La Jolla, San Diego, California 92093, USA

hDepartment of Nanoengineering, University of California San Diego, La Jolla, California 92093, USA

iDepartment of Civil and Environmental Engineering, University of California, Davis, California 95616, USA

jDepartment of Chemistry, University of Wisconsin, Madison, Wisconsin 53706, USA

† Electronic supplementary information (ESI) available. See DOI: https://doi.org/10.1039/d3ea00060e

© 2023 The Author(s). Published by the Royal Society of Chemistry

Environ. Sci.: Atmos., 2023, **3**, 1513–1532 | 1513

1. Introduction

The state in which a cloud exists in the atmosphere, as composed of liquid or frozen droplets or both (so-called mixed-phase), is important to both weather and climate due to its impacts upon precipitation and radiative forcing.[1] The sizes and compositions of particles, in combination with cloud dynamics that drive water vapor supersaturation at cloud base, controls the number of droplets initially formed in a cloud. This droplet number concentration can sometimes represent a major fraction of all particles, especially those at sizes above a range from about 0.06 to 0.14 μm, determined more by cloud supersaturation than by aerosol composition.[1–4] Clouds commonly supercool below 0 °C and liquid droplets may persist as clouds grow to altitudes where the homogeneous freezing temperature for small cloud droplets is achieved (*e.g.*, 235 K). The initiation of the ice phase, and subsequently ice crystal concentrations formed at more modest cloud supercooling are controlled by a rare population of aerosol particles termed ice nucleating particles or INPs for short.[5] For emissions specifically from the oceans in the form of sea spray aerosols (SSA) produced by bubble-bursting, the fraction of all particles emitted that are INPs depends on temperature but can be typically 1 in 10^6 at 248 K and 1 in 10^8 at 258 K.[6] On the basis of surface area normalization of INP concentrations, often termed the surface-active site density (n_s), ocean-emitted INPs are 10^3 to 10^4-fold less efficient than mineral dust INPs.[6,7] For this reason, INPs over equatorial and mid-latitude ocean regions are posited to be controlled by mineral dust transport *versus* marine INP emissions,[8,9] and hence the most likely place where marine emissions may control INP budgets is over remote ocean regions such as the central Southern Ocean.[10]

The composition of marine INPs appears to be dominated by organic materials that are sourced from both particulate organic carbon INPs (likely microbial) and from long-lived dissolved organic macromolecules.[11] We refer to these herein as SSA INPs because they emanate from the emission of SSA in the bubble-bursting process at the ocean's surface during wave-breaking. The latter category of SSA INPs has been parameterized by differentiating these common emissions from the more episodically enhanced particulate INP emissions.[7] Numerical frameworks for encapsulating the totality of marine INP emissions have been proposed, assuming heterotrophic bacteria and marine biopolymer aggregates as target entities.[12] While some candidates for marine ice nucleating molecules and microbes have been identified,[11,13,14] it is likely those of greatest relevance as INPs have not yet been characterized except in a large category sense.[15] Nevertheless, given the inferred organic makeup of marine INPs, a question arises as to the lifetime of these INPs under the action of atmospheric oxidation processes.

It is known that radical-initiated heterogeneous oxidation of organic and inorganic matter can alter the composition, size, density, optical properties and cloud activation properties (at least as concerns hygroscopicity, which controls cloud condensation efficiency) of atmospheric particles.[16] Heterogeneous oxidation increases the oxidation state of particulate carbon in pre-existing organic aerosols, but the amount of particle-phase carbon can decrease with oxidation, due to fragmentation reactions that form volatile gas phase products.[17] In this manner, functionalization of organics is altered. For oxidation occurring in the presence of reactive gases, condensation on pre-existing aerosols may also occur.

These processes frame what can happen for sea spray aerosols, which encounter OH radicals in the daytime, resulting in three distinct possible aerosol populations.[18] Original (nascent) SSA particles are modified *via* reactions in existing organic coatings that include proteins, amino acids and phospholipids[19] and condensation of biogenic volatile organic compounds and their oxidation products to produce a population of aged SSA, while the gas phase oxidation products may also produce a newly nucleated population of secondary organo-sulfate marine aerosols. The combined population of aged nascent SSA and secondary particles is commonly referred to as secondary marine aerosols (SMA). Using oxidation methods similar to those we will apply in this study, Trueblood *et al.* (2019) demonstrated through Raman spectral data on aged sea spray particles that OH oxidation reactions in the net significantly lower the amount of organic matter found in supermicron SSA particles during phytoplankton bloom conditions.[20] Direct evidence of fragmentation reactions due to heterogeneous OH reactions with SSA were identified. From a number standpoint though, SMA is typically dominated by particles produced at sizes below 100 nm providing a vital pathway toward the production of cloud condensation nuclei in the marine boundary layer based on both laboratory and field studies.[21,22]

The impact of oxidation on SSA INPs has not yet been investigated. It has been demonstrated that photochemical processing of dissolved organic matter (DOM) over a period of ~4–6 days decreases the INP content in freshwater suspensions, inducing up to a 4 K decrease in the temperature where 50% of DOM droplet suspensions freeze.[23] However, it is unknown if the responsible photomineralization process that converts organic carbon to acidic molecules in freshwater also occurs for what would be very different INPs from SSA in the atmosphere. Since INPs are rare within the overall SSA aerosol population, other organics could be involved that include surface active materials, marine gel components, vesicles and viruses.[24,25] There is no expectation that SMA produced from nucleation of new particles, with mode sizes well below 100 nm, represent an INP source for mixed-phase cloud conditions. In prior studies investigating freezing of other secondary organic aerosols, such as those formed from oxidation of α-pinene, any heterogeneous freezing efficiency has been difficult to discern and freezing primarily occurred within the range of relative humidity conditions that lead to homogeneous freezing of dissolved particles at temperatures below 235 K.[26,27] Due to this evidence for other secondary aerosol types, we will assume no involvement pure secondary marine aerosols as INPs in our studies focused at temperatures >243 K. In this study, we instead seek to learn more about both the influence of oxidation on SSA INPs that may include altered organics (we will refer to this as "aged" SSA), and to seek new information on these target organics. In this effort, we presume to be focused on aged nascent SSA.

2. Methods

2.1 Wave channel production of primary sea spray aerosols

The measurements reported herein were conducted as part of the Sea Spray Chemistry and Particle Evolution (SeaSCAPE) study, as detailed in Sauer *et al.* (2022)[28] and shown in the schematic of Fig. 1. The core facility for this study was the Scripps Institution of Oceanography (SIO) wave channel, a 33 m long and 11 800 L device that uses an electromagnetically driven paddle and a submerged fiberglass beach located midway down the channel to amplify waves to the point of breaking.[28–30] Continuous breaking waves generate entrained bubbles that have been shown to possess a similar size distribution and residence time as those in the ocean.[28] Sampling ports for aerosol studies were located downstream from the breaking waves. The system is sealed from all but minor contamination with room air and supplied with particle-free air to fill the head space over breaking waves.[28] Primary SSA emissions were thus isolated for analysis. Condensation particle counters were used to measure total particles upstream and downstream of the wave breaking point, and those upstream typically represented no more than 2% of typical total SSA particle numbers of 250 cm^{-3}.[28] The wave channel was equipped with fluorescent lights to provide a light flux. While at a reduced level compared to the flux of photosynthetically active radiation found over the open ocean, it was sufficient for photosynthetic organisms to grow in the seawater. Results herein are based around what was referred to as bloom 3 during SeaSCAPE. For this bloom, the 33 m wave flume was first filled with seawater. After 1–3 days, during which the seawater temperature equilibrated, nutrients were added. The fluorescent lights were operated for ~15 h each day, to simulate real diel patterns and drive biological activity that resulted in growth and decay of the bloom. Wave-breaking occurred throughout each mesocosm (day and night), producing nascent aerosols and enhancing gas exchange. High time-resolution instrumentation sampled continually, either the nascent aerosols and gases or photochemically-processed aerosols and gases. While not shown in Fig. 1, two oxidation flow reactors (OFRs) were set up equivalently to sample both aerosols and gases, with one feeding aerosol and CCN measurements (not shown), and the other feeding INP measurements and other offline collections of particles for analytical methods (shown). Ozone was scrubbed following the OFR using a carulite 200-filled diffusion drier (Ozone Solutions).

2.2 Standard aerosol measurements

Aerosol size distributions of nascent SSA after the wave breaking position were measured using an aerodynamic particle sizer (APS, Model 3321, TSI Inc) sizing from 542 nm to 20 μm (aerodynamic) and a scanning mobility particle sizer (SMPS, Model 3938, TSI Inc) equipped with a DMA (DMA 3081, TSI Inc) and a soft X-ray Neutralizer (Model 3088, TSI Inc), sizing particles from 25 to 705 nm.

2.3 Ice nucleation measurements

Online and offline INP measurements were made on both nascent and OFR particle streams at different times, as shown in Fig. 1. The online measurements served primarily for monitoring variations of INP concentrations over time during a bloom at one temperature and for assessing changes in concentrations under exposure to a variable daily set-point level of oxidative exposure in the OFR. A low temperature, 243 K, was
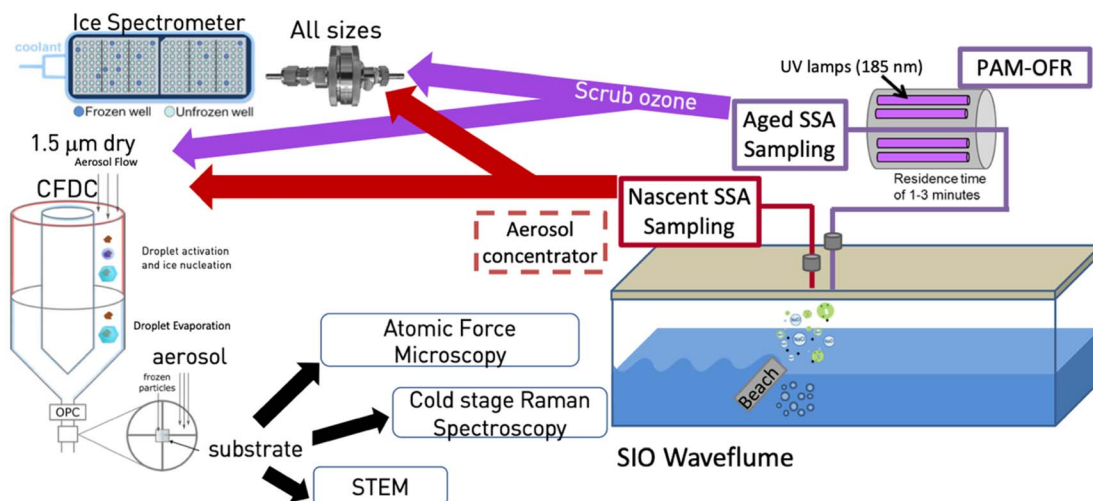

Fig. 1 Schematic of experiment. Aerosols were produced from artificial beach-induced breaking of waves and subsequent bubble generation in the SIO wave channel.[29] (Prather et al., 2013) Particles were sampled for INPs either through an inlet drawing only nascent SSA or first passed through an OFR, as described in the manuscript. The nascent sampling line used a large diffusion dryer prior to transit of particles to the CFDC and IS filter. The OFR line was not dried until after particles passed through the OFR, whereupon ozone was scrubbed by a carulite diffusion dryer and then by a single silica gel diffusion dryer for the IS filter and silica gel and molecular sieve diffusion dryers for the CFDC. The ice nucleation instruments (ice spectrometer, CFDC) and analytical methods applied to substrate-collected INPs from the CFDC are also shown and are described fully in the manuscript.

chosen for this analysis to activate high numbers of INPs for subsequent INP analytical collections, and this was further assisted by an aerosol concentrator, as discussed below. Offline measurements served a similar purpose in monitoring INP concentrations over time using larger volumes of collected air, which also allowed for obtaining INP concentrations *versus* temperature, while sampling the nascent or OFR-processed particle streams.

2.3.1 Continuous flow diffusion chamber. Online measurements were made using a Colorado State University (CSU) continuous flow diffusion chamber (CFDC),[31,32] a vertically-oriented, geometrically-cylindrical, ice-thermal diffusion chamber exposing particles to nearly steady-state temperature and relative humidity conditions at a flow rate of 1.5 L min^{-1} between two ice-coated walls. Sample air from the wave flume passed first through three diffusion driers (two silica gel and one molecular sieve), then through a pair of matched single-jet impactors to remove dry particles larger than 1.5 μm diameter (50% aerodynamic cut-size diameter) before entering the chamber. For this study, water supersaturation in the chamber was typically held between 4 and 8% (or water relative humidity, RH_w, of 104 to 108%) to activate particles into water droplets, emphasizing measurement of ice nucleation in the immersion freezing mode for consistency with the offline immersion freezing measurements.[33,34] The CFDC residence time for ice nucleation was ~5 s, with an additional 2.5 s of exposure to water subsaturated conditions to evaporate water droplets to aerosol sizes, leaving ice crystals at sizes exceeding ~4 μm as measured by an optical particle counter (OPC).[32] The same OPC also measured aerosol particle concentrations at sizes larger than about 0.3 μm. The temperature of the aerosol lamina, which is sheathed in HEPA-filtered air, was set to 243 K for SeaSCAPE. This was motivated by the expected relatively low INP concentrations and because of the need to simplify the range of parameters used while meeting objectives to collect INPs for offline analyses. The CFDC sample flow was filtered (HEPA) for 5 min of every 15 min to provide instrument background counts, quantifying low level frost emission during operation.[33] INP concentrations and confidence intervals were calculated based on a Poisson model for rates of detection of INPs during ambient sample and surrounding filtered-air periods. In this way, background correction and statistical confidence are folded into the initial analysis step.[32]

Collection of activated INPs was performed for analyzing the impacts of oxidation on INP morphology and composition. Ice crystals >3.8 μm (50% aerodynamic cut-size diameter) exiting the CFDC chamber were collected onto various substrates for analysis using a single jet impactor.[35] Subsequent analytical methods are described in the next subsection. To enhance numbers of INPs collected for analyses, the nascent sample air was sent through an aerosol concentrator prior to sampling by the CFDC.[36] The aerosol concentrator (MSP Corporation, model 4240) sampled *via* a 3/4″ carbon-impregnated conductive tubing line (transitioning to a custom-machined cone at the 4″ entry to the concentrator) from the wave flume at 250 lpm, and the concentrated-flow at 1.5 lpm was drawn by the CFDC. Enhanced concentrations occur primarily for particles at diameters

>500 nm, but with a size-dependent enhancement ratio (concentration factor, or CF) up to particle diameters larger than about 1 μm.[37,38] Consequently, the benefit of the concentrator for statistical sampling of INPs is somewhat counteracted by the interactions of the size-variable CF with the uncertain size distribution of sea spray produced INPs. The concentrator necessarily emphasizes selection of particles with wet diameters larger than 1 μm, and hence dry sizes above about 0.5 μm and up to the dry cut-size of the CFDC upstream impactors.

While a CFDC is designed to easily accommodate water vapor consumption by growing liquid droplets and ice crystals for most situations encountered in the atmosphere, laboratory simulations involving high CCN numbers activated at the high water vapor supersaturations employed can ultimately tilt the water balance toward consuming the supersaturation and thereby impact INP activation, which is known to be sensitive to the level of water supersaturation in the CFDC for artifactual reasons.[33] Using a variety of seed particles for initiating ice formation at varied concentrations up to 10^7 cm^{-3}, Levin *et al.* (2016) determined correction factors for INP concentrations in scenarios that involve high concentrations of seed particles.[39] These corrections could be relevant for sampling from the OFR in SeaSCAPE, since total particle numbers reached 80 000 cm^{-3} for some OFR settings,[28] exceeding the ~10 000 cm^{-3} threshold where water vapor consumption impacts become evident in the CFDC.[39] At 80 000 cm^{-3}, the INP underestimate could be up to a factor of 3.[39] However, that prior study investigated INP underestimation using mineral and wildfire aerosols as the seeds, and none of those aerosol distributions (mode diameters > 0.1 μm) were dominated by particles as small as SMA, with a mode diameter at below 20 nm. For a particle with a diameter of 10 nm and a hygroscopicity parameter of 0.1 as appropriate for small organic aerosols, critical supersaturation for CCN activation is 10%,[40] much higher than values used in CFDC processing. Further, losses of smallest particles in upstream sample tubing and the CFDC inlet system will lead to substantial losses of particles, >50% at 25 nm for one prior study,[41] and >80% at 15 nm in the same calibrations referenced in that paper. Hence, it is unlikely that small mode SMA would ever be activated as droplets in the CFDC, and so no INP corrections were applied in this study. This is supported by results on the few days when OFR exposure had no discernible impact on INPs, as discussed later.

2.3.2 Ice spectrometer (IS). Nascent particles and aged particles from the OFR were also passed through a single silica-gel diffusion drier and collected on filters for processing with the CSU Ice Spectrometer (IS) instrument (Fig. 1). The concentrator was not used for any IS collections. The IS and its experimental protocols, including cleaning of the Pall aluminum inline filter holders and 0.2 μm pore diameter polycarbonate Nuclepore filters (and 10 μm pore backing filters), have been described in numerous publications for processing a diverse array of aerosols, including SSA.[7,32,34] The device is used to process water samples and aerosol suspensions for measurements of immersion freezing INP temperature spectra. In this study, suspensions of particles, as well as 20- and 400-fold dilutions of the suspensions, were created from filter

samples following agitation in 7 mL of 0.1 μm-filtered deionized water. Droplet (50 μL) arrays were cooled at 0.33 K min^{-1} and the freezing of wells were identified from images through a LabVIEW interface. Lowest measurable temperatures range from 246 to 243 K. Blank corrections for INPs from the DI water used for aerosol resuspension, determined for aliquots distributed in the same array plates as daily samples, were applied before conversion of data to cumulative INPs per suspension water and per standard liter of air sampled.[42] A suspension from a clean filter was also tested and showed little contribution, so corrections were not made for this potential contamination factor (Fig. S1†). Confidence intervals (95%) for binomial sampling were calculated based on Agresti and Coull (1998).[43] Sample volumes for nascent and aged SSA were approximately 1800 and 900 L, respectively, based on sampling for 4 h at 6.5 sL min^{-1} for nascent collections and 2.5 h at 5.2 sL min^{-1} for OFR-processed particles. The lower flow for OFR-passed SSA was required to keep the total flow through the sample lines the same for sampling off both the nascent and OFR lines, the latter being split between the IS filter and CFDC. Considering sampled volumes of air, detection limits were ~0.001 INPs per L.

For SeaSCAPE, IS filter samples of nascent SSA were intended as PM10 collections, but this was modified by line losses. Using the line physical dimensions and bends, calculated transmission efficiency *versus* geometric particle size to the filter *via* the nascent sample lines is shown in Fig. S2,† where it is seen that 50% transmission was expected at 4 μm and 10% at 6 μm. Transmission to the IS filters through the OFR line will be discussed in the next section. The use of upstream impactors for the CFDC necessarily created a size bias with the IS filter collections when sampling on nascent lines. Whereas for the CFDC the distribution was limited to aerodynamic diameter below 1.5 μm (50% point), or a physical diameter below about 1 micron (Fig. S2†), the IS filters on the nascent line favored larger particles since they included more of the full surface area and volume mode of SSA (see next section).

2.4 Aerosol loss factors in the OFR and their implications for this study

As a preface to ice nucleation results, it is also necessary to discuss the influence of aerosol losses that occurred in the standard configuration of the PAM-OFR. Due to logistical factors, calibrations to test for aerosol transmission losses through the instrument as a function of particle size were not possible until after the campaign ended. To perform these tests, tubing configurations and runs were reproduced as closely as possible and total flow rate was matched to that used in SeaSCAPE. Tubing downstream of the OFR in SeaSCAPE was quite limited, so its impact on distributions sampled by the CFDC and IS filter were not exactly simulated in the loss test. Sea spray particles were generated with a Marine Aerosol Reference Tank (MART), which uses a plunging water mechanism and is intended to reproduce aerosol distributions that mimic the wave flume and nascent SSA.[42] Hence, we do not expect any bias from using the MART for this calibration test.

The calibration configuration and results are shown in Fig. S3 and S4,† respectively. The SMPS and APS data were merged by converting the aerodynamic diameter of the APS to physical diameter, and for this purpose dried SSA were assumed to be spherical particles with a density of 1.8 g cm^{-3}.[44] There were not significant particle losses until sizes between 2 and 3 μm (50% transmission at 2.8 μm, 10% transmission at 3.8 μm). This means that the CFDC should have captured aerosols and INPs without extra losses when using the OFR. However, at sizes >3 μm, significant losses of aerosol surface area and volume occur, which influenced IS filter results presented here. With higher transmission on the nascent line to the IS, much more aerosol surface area and volume was captured in those samples compared to sampling *via* the OFR. As surface area and volume are known to bear relation to marine INP concentrations,[7,45] the use of the OFR was imperfect for studying the influence of aging on INPs that may reside at larger sizes and were captured by IS filters on the nascent line. Discussion of results in subsequent sections takes this consideration into account.

The consequence for these studies is that the CFDC data are the primary data for demonstrating oxidation impacts, albeit restricting analyses primarily to INPs active at 243 K (excepting use of the cold-stage Raman). Nevertheless, this means that the analytical studies should have had no bias other than the fact that they emphasize particles generally smaller than 1.5 μm dry aerodynamic diameter, a fortuitous decision for these studies. The IS data, while intended to provide inference to oxidation impacts across the full INP temperature spectrum, including larger SSA, must be considered with more care. We discuss an experiment of OFR transmission of INPs with the PAM lamps off in the next section.

2.5 Analytical methods

A key feature of the design of the experiments as represented in Fig. 1 was the concept to maximize collection of INPs from the CFDC for physical and chemical analysis. Analyses of single INPs included elemental composition and size/morphology by scanning transmission electron microscopy/energy dispersive X-ray spectroscopy (STEM/EDX), micro-Raman spectroscopy with cold-stage capabilities for reactivating INPs, and atomic force microscopy (AFM) for morphology and phase state. The concept was that if the CFDC INP concentrations were 100 per liter at 243 K (following the aerosol concentrator), collection over a 5 hours period concentration would accumulate 45 000 INPs to a sample substrate for use in analysis. This would allow potential statistical assessment of morphology, phase state and elemental compositions active at 243 K. Reactivation of INPs in the micro-Raman system provided for extended analysis of compositions of INPs active at higher temperatures than could be collected in sufficient quantities from the CFDC. A key limitation to mention about the analytical studies is that they are restricted to the sizes assessed by the CFDC, those below the 50% dry aerodynamic cutoff diameter of 1.5 μm.

2.5.1 Scanning transmission electron microscopy/energy dispersive X-ray spectroscopy (STEM/EDX). For analysis of CFDC-collected INPs by STEM/EDX, the CFDC ice crystal

© 2023 The Author(s). Published by the Royal Society of Chemistry

Environ. Sci.: Atmos., 2023, **3**, 1513–1532 | **1517**

impactor was fitted with 3 mm, 200 mesh Ni or Cu support, C/formvar coated grids (SPI Supplies, West Chester, PA). Grids were stored clean and dry after collection and subsequently analyzed at CSU on a JEOL JEM-2100F 200 kV scanning transmission electron microscope with an energy dispersive X-ray spectrometer (Oxford Energy Max 80) system. Use of blank grids (installed in CFDC, but not exposed to sample flow) and obtaining background X-ray elemental spectra from particle-free regions of sampled grids provided a means to set detection limits and exclude potential artifacts.[32] Analysis of up to 50 particles from each grid was attempted, and particles were categorized based on spatial mapping of their detected elements and morphology. Categories were made to be as equivalent as possible to the morphological categorizations of the AFM analyses (see below). This included dried particles that had NaCl cores with shells of other inorganic materials and organic carbon (core–shell), rounded-morphology particles, and irregularly shaped particles. These will be discussed further in the Results section (3.3.1).

2.5.2 Micro-Raman spectroscopy of INPs. Following Mael *et al.* (2019; 2021), micro-Raman spectroscopy was used to provide insights on functional groups and chemical species within individual particles, with a special focus on re-activation of INPs.[46,47] The primary contribution of these cold-stage Raman studies was to be able to focus on the onset freezing temperatures and compositions of INPs that activate at much higher temperatures than could be assessed by the CFDC and its associated TEM collections. The reason is that the substrate collected all INPs activating at a nominal temperature of 243 K from the CFDC, but over hours of operation. With between 10 000 and 100 000 INPs collected *via* use of the aerosol concentrator over periods up to 5 h, and a typical order of magnitude decrease of SSA INP concentrations per 5 K warming,[6] it was thus possible to assess INPs activating to perhaps as warm as 263 K. Nascent and aged SSA INP collections from the CFDC were collected onto quartz discs (Ted Pella, 16001-01) coated with Rain-X to promote hydrophobicity. Nascent samples were collected during SeaSCAPE phytoplankton bloom 3 on four days and aged samples three other days spanning the study period. These samples were dehydrated and returned to ambient temperature following collection. For analysis, substrates were placed at ambient relative humidity into an environmental cell (Linkam, LTS 120). The cell was coupled to a micro-Raman spectrometer (Horiba, LabRAM HR Evolution) for spectral analysis.[44] Using the 100× SLWD objective, Raman spectra of 30–90 particles per substrate were collected between 400 and 4000 cm^{-1} with five, nine-second exposures averaged per scan. Spatial coordinates of the vertices of the substrate were recorded along with the x and y coordinates of particle spectra with unique and distinguishable spectral features. Following this, water uptake/loss and freeze/thaw cycles were conducted on 100 μm^2 subsections of the substrate. Visually assessing one subsection of the substrate, the RH$_w$ within the cell was increased to 90% by altering the ratio of dry to humidified N$_2$ flowing into the cell, leading to water uptake and formation of droplets on the impacted particles. Once hydrated, ice nucleation measurements within the subsection were made by

decreasing the temperature in the cell and visually assessing the phase state of the particles. Once the first clear optical change consistent with ice formation occurred, the temperatures and coordinates of the first particles to freeze were noted (as were any other particles freezing before 250 K), after which the temperature and relative humidity was returned to 298 K and 0%, respectively, constituting one water uptake/loss and freeze/thaw cycle. Once dehydrated and returned to ambient temperature, Raman spectra of the noted freezing particles were collected. Additional water uptake/loss and freeze/thaw cycles were repeated across the substrate within each 100 μm^2 subsection for all samples. Accounting for all freezing events, average onset freezing temperature could be determined for each sample, for both nascent and aged SSA INPs. Raman spectra could also be obtained to assess INP compositions/types. We will focus most discussion of results on INPs identified to freeze at >250 K, as below this temperature it was necessary to separate INP freezing from other particles that froze adjacent to them following ice growth on the substrate.

2.5.3 Single particle atomic force microscopy (AFM) measurements of the morphology and phase state of INPs. Morphology and phase state of CFDC-collected nascent and aged INPs were determined using atomic force microscopy (AFM) measurements. The sample analytical methods as applied for total SSA measurements reported for SeaSCAPE in Kaluarachchi *et al.* (2022) were applied for this study.[48] Collections of INPs in the CFDC used the same single jet impactor device as used for TEM and micro-Raman studies, but hydrophobically coated (Rain-X) silicon substrates (Ted Pella, Inc.) were substituted for the up to 5 h collections. The substrates were stored in clean Petri dishes and kept inside a laminar flow hood (NuAire, Inc., NU-425-400) at an ambient temperature (293 to 298 K) and pressure prior to AFM measurements. Focused AFM analyses guided collections on 08-07-2019, when both nascent and aged INPs were collected on AFM substrates for analysis over the volume-equivalent diameter range of 0.1–1.0 μm. This day represented the peak of heterotrophic bacteria concentrations, following the peak of chlorophyll-*a* (Chl *a*) on 08-03-2019 during the third SeaSCAPE phytoplankton bloom.

A molecular force probe 3D AFM (Asylum Research, Santa Barbara, CA) was used to image individual INPs at ~20% RH$_w$ and ambient temperature (293 to 298 K) and pressure following Lee *et al.* (2019; 2020).[49,50] A custom-made humidity cell was used to control RH$_w$, and phase state measurements were then collected at 20% and 60% RH$_w$. For each RH$_w$ value, a waiting time of at least 10 min was given prior to each AFM measurement to ensure the substrate-deposited particles were in the thermodynamic equilibrium with surrounding water vapor.[49] These RH$_w$ values were selected as a benchmark based on previous phase state studies on sucrose that show solid-to-semisolid and semisolid-to-liquid phase transitions at ~20% and 60% RH$_w$, respectively.[51,52] Silicon nitride AFM tips (MikroMasch, model CSC37, tip radius of curvature ~10 nm, nominal spring constant 0.5–0.9 N m^{-1}) were used for AFM imaging and force spectroscopy measurements. AFM AC mode imaging was used to collect height images of individual particles to determine their morphology, and quantify the volume-

1518 | *Environ. Sci.: Atmos.,* 2023, **3**, 1513–1532

© 2023 The Author(s). Published by the Royal Society of Chemistry

equivalent diameter, as described in prior studies.[49,51] Approximately 50 individual particles were studied for each sample type (nascent and aged) accumulated for the different collection days, and the relative abundance (*i.e.*, average with one standard deviation for fraction of particles) of identified main morphological categories (rounded, core–shell, prism-like, core–shell with inclusions, and aggregate) were compared between two nascent and aged samples.

For phase state identification, AFM force spectroscopy (*i.e.*, force plots) were determined for individual INPs at ambient temperature (293 to 298 K) and pressure by probing at the shell region of core–shell, at the shell and inclusion regions of core–shell with inclusions, and approximately at the center of prism-like and rounded particles. A maximum force of 20 nN and scan rate of 1 Hz was used, and at least five repeated force plots were collected for each particle at a particular RH_w. The collected force plots were then used to quantify the viscoelastic response distance (VRD, nm), which can be related to viscoelastic nature of a solid (higher VRD values generally correspond to lower viscosity), and the relative indentation depth (RID, ratio of the indentation depth over the particle height) for an individual particle at a particular RH_w.[51,53] A previously reported framework, based on the VRD and RID measurements, was then utilized to identify the phase state of each particle at ~20% and 60% RH_w.[52] Approximately 10 or more individual particles for each morphology type from both samples were investigated.

Since the AFM approach is limited to a finite number of particles, a statistical analysis to assess statistical significance of the AFM measurements was employed. In particular, probability distribution curves associated with the likelihood of sampling one of the five particle morphology types, or one of the three phase states, were generated using the Markov chain Monte Carlo method.[54,55] To generate these distributions, a "true" population of 10 000 particles was generated with the number of particles of a given type equal to the measured value for a given sample type or a phase state. A random sampling

without replacement of 10 000 sub-populations of actual number of particles from the true distribution was then performed, and the results yielded the probability distributions for each particle type. Next, by fitting the probability distribution plots into the Gaussian equation, an average with one standard deviation for fraction of particles from each morphological type, or one of three phase states was determined.

3. Results and discussion

3.1 Characteristic action of oxidation on INPs

3.1.1 CFDC results. Two daily timelines of CFDC measurements over the course of the bloom experiment are shown in Fig. 2. The two examples include the only day within SeaSCAPE bloom 3 when the OFR was operated with the lights off, due to concerns regarding particle losses that arose during the study. The shared use of the OFR only permitted one experiment of this type with the CFDC and IS filters toward the end of bloom 3, shown in Fig. 2a. An experiment with the lamps operating to simulate 8 days of equivalent oxidative processing is shown in Fig. 2b. Measurements with the CFDC always began with a period of sampling nascent INPs, followed by a period sampling the line through the OFR, sometimes bookended with a second nascent sample, a period sampling nascent INPs *via* the aerosol concentrator to facilitate collections of INPs (CFDC) for offline analyses, followed by a final period measuring nascent particles without the concentrator. Aerosol and INP concentrations in Fig. 2a confirm that there were no inherent losses involved in use of the OFR prior to CFDC measurements, consistent with the absence of losses of particles in its size range noted in the MART calibration test (Section 2.4). Further, aerosol concentrations from the CFDC OPC at optical dry sizes between 0.5–1.5 μm were the same whether sampling through the OFR with lamps on (Fig. 2b) or off (Fig. 2a). Possible size-sorting enhancement of aerosol concentrations at specific sizes entering the CFDC was noted (Fig. S5†) when using the OFR *versus* the nascent sample line. The source of this is
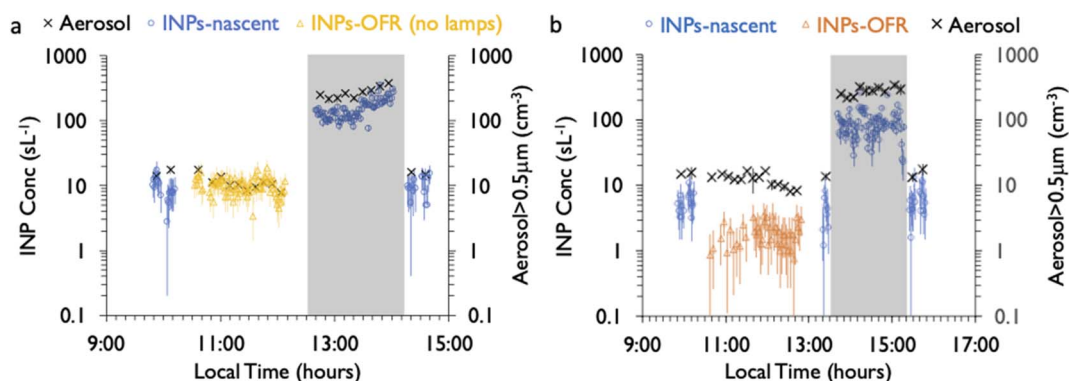

Fig. 2 Timelines of typical daily CFDC measurement cycles, here for (a) August 6, 2019 and (b) August 8, 2019. All measurements are at a temperature of 243 K and nominal water supersaturation of 6%. INP concentrations (1 min) are distinguished for periods sampling nascent (blue circles and confidence intervals) and OFR (gold triangles and confidence intervals) sample streams. Aerosol concentrations measured by the CFDC OPC are plotted (black x's and confidence intervals) as 10 min averages of particles with dry equivalent spherical diameters between 0.5–1.5 μm. The grey shaded region indicates the period of use of the aerosol concentrator. The two dates are distinguished by the operation of the OFR without lamps powered in (a) and with the lamps on in (b), simulating 8 days of atmospheric aging.

unknown but must involve the mixing and passage of air within the OFR. The consequence was enhanced aerosol concentrations of more than 2 times in the dry size range from about 1 to 1.4 μm. This appears to have had no other detrimental effect on the INP results. Fig. 2b then demonstrates the impact of oxidation during an experimental day with the OFR lamps on, and a consequent loss of INP freezing efficiency (*e.g.*, a degradation of INP concentrations, all else being equal). A dramatic 3 to 15-fold reduction of INPs is noted in comparison to Fig. 2a, and this occurs despite no significant impact on aerosol concentrations.

Finally, the impact of the aerosol concentrator on INP and total particle concentrations is also noted in Fig. 2. Aerosol concentrations at sizes larger than 0.5 μm increased by a typical factor of 20 times, referred to as the concentration factor (CF). The value of CF reflected changes in aerosol emissions and sizes over the course of the phytoplankton bloom experiment, ranging from 5 to 20 on different days. This may be understood to be a consequence of the size-dependent concentrating characteristics of the device. Fig. S6† shows the CF value interpreted from the full aerosol size distribution measured by the CFDC OPC, where CF ranges from ~10 for a dry aerodynamic particle diameter of ~0.4 μm, up to a maximum value of about 150 for a dry diameter of 1.5 μm, the latter value consistent with previously published values and also with the maximum CF for the input flow rate of 230 L min^{-1} lpm and output of 1.5 L min^{-1}.[32] The pre-impactor cut size of 1.5 μm is also evident in the count distributions in Fig. S6,† roughly separating aerosol (to the left) and particles that grow to ice sizes (to the right), for which the "dry" calculation of size is of course not valid (*i.e.*, they were actually larger than 2–3.5 μm). In the absence of a uniform CF over all sizes, we consider the analytical studies of collected INPs to be representative for the classes of INPs in the size range above 0.5 μm, but we do not analyze for actual size-dependent compositions and OFR impacts that may exist.

3.1.2 IS results. Results of inline filter IS measurements of INPs in the experiment with OFR lamps off on August 6, 2019 are shown in Fig. 3a. The IS spectra were seen to lose many of their INPs after passing through the OFR, implying both that there are many INPs at sizes larger than the 3 μm effective dry particle cut-size of the OFR and that inline filter OFR measurements require these losses to be taken into account. Correction is clearly T-dependent in this single test of OFR losses, which likely reflects the size and temperature-dependent efficiency of marine INPs. Using linear regressions on the INP data from nascent and OFR lights-off conditions, a loss ratio was determined that was then applied uniformly for all IS-OFR measurements to determine the proportion of INP loss attributable only to physical losses in the OFR. We must note, however, that the use of a single calibration of particle and INP losses may not represent daily differences that might occur, for example, due to relative humidity changes in the wave channel head space, or changes in the size distribution of produced particles and/or INPs. Therefore, we expect imperfect attribution of OFR oxidation impacts using IS data, represented as an increment on INP reduction after physical losses (Fig. 3b). August 7 was the date of the largest additional decrement of INP activity, motivating its use here as an idealized example. However, as shown in Fig. S7† OFR impacts were sometimes not easily discernible from the large reduction (10× at 248 K) predicted due to physical OFR losses. As we will show in the next section, this made IS sampling from the OFR particle stream less conclusive and useful toward understanding oxidation impacts on larger particles that the CFDC did not interrogate.

As mentioned, a secondary result of significance from the noted loss of INPs in the OFR is that it indicates that inline IS filter collections during this particular phytoplankton bloom mesocosm were dominated by INPs at dry particle diameters larger than the CFDC upstream impactor cut-size (1.5 μm aerodynamic). This is not surprising and mimics the conclusions from prior experiments wherein jet and film drop emissions of INPs were isolated to show that supermicron SSA INPs
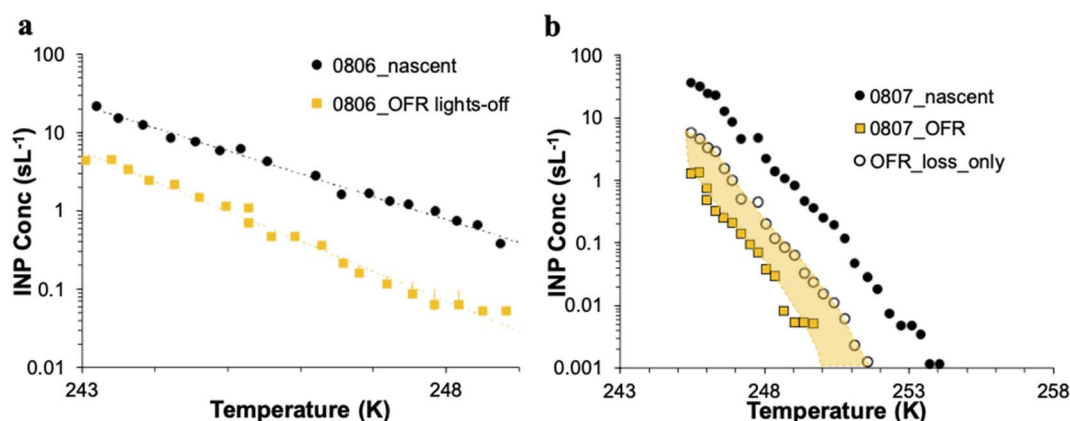

Fig. 3 INP data demonstrating particle loss impacts on IS temperature spectra when passing through the OFR with the lamps off on August 6, 2019, in (a), which was quantified by linear regressions and used to predict physical particle losses during lamps–on OFR operation, as done in (b) for data on August 7, 2019. Oxidation loss of INP activity is indicated in (b) by the yellow shading of the additional decrement of INP activity that occurred when the OFR lamps were operated.
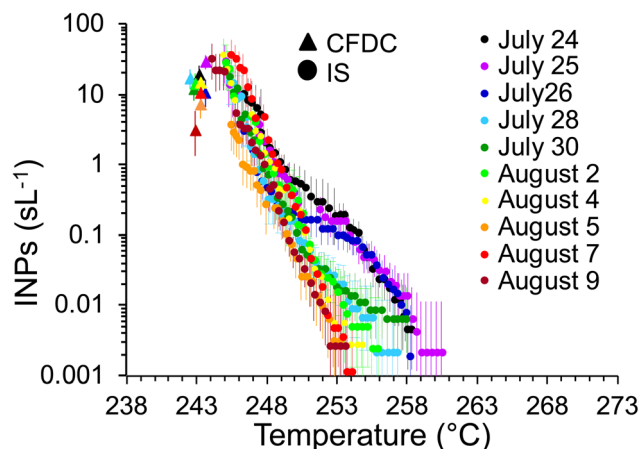
Fig. 4 Proximal (in time) data from the same days of SeaSCAPE, from the CFDC operating near 243 K and IS INP temperature spectra. The CFDC data are averaged over the periods of nascent sampling each day. The error bars indicate 90 and 95% confidence intervals for the CFDC and IS data, respectively.

can dominate over INP contributions from the submicron range.[45] Further proof is evident when comparing the IS and CFDC INP concentrations on days when both methods sampled

nascent INPs, shown in Fig. 4. Although the two data streams do not have an overlapping temperature regime of measurement, there is a clear low bias of CFDC INPs compared to IS INP concentrations, exemplified by the disconnect of the projected trend of IS data toward 243 K and the CFDC data collected there. This discrepancy is not always seen in ambient marine air, nor in some previous wave flume studies,[6,56] but has been noted as a feature of CFDC and immersion freezing data at these temperatures in other sampling scenarios.[31]

3.2 Summary of oxidation impacts on INP number concentrations

A comprehensive summary of all CFDC and IS data for nascent *versus* OFR treatments is compiled in Fig. 5. The caption of Fig. 5 details the symbol notation used.

The CFDC timeline of daily average INPs at 243 K from nascent and oxidized particle streams (dry particles below 1.5 μm aerodynamic diameter) demonstrates clear impacts of oxidation that range from nearly none on July 29 to a 5-factor degradation on July 24, the first day of measurements after fresh water was added to the wave flume (Fig. 5a). Equivalent days of oxidation, as per calibrations done during the study, were 3.2, 4.6, 6.0, and 7.9 d, but are labeled to the nearest full day of

Fig. 5 Timeline of oxidation impacts as inferred from CFDC INP data at 243 K (a) and IS INP data at 248 K (b). Results are shown as daily average INP concentrations for nascent (filled circle points) and oxidized INPs (filled triangle points), with (closest integer) days of equivalent aging indicated below each experimental day. Uncertainties are 90% confidence intervals for CFDC data and 95% binomial confidence intervals for the IS measurements. For the CFDC data, a decremental impact on INP concentrations is indicated by the yellow shaded region. For IS data, the decremental impact of particle losses alone (open circles), based on the lamps–off calibration experiment on August 6 is used to estimate the inferred decrement (yellow shading) or (paradoxical) increase (red shading) in concentrations attributable to oxidation. On August 6, the no lamps results are indicated by open triangles (white fill). Other events over the course of the bloom are indicated with text along the timelines for panels (a and b).[21]

oxidation in Fig. 5. Full one-minute CFDC data, including times on the aerosol concentrator, are shown in Fig. S8.† While the impact of changing oxidation on any given day could not be determined because only one oxidation setting was possible per day during these studies, no obvious relationship is notable. Average losses were a factor of 2.0 for the bloom series (standard deviation bounds from 1.3 to 4.1). These are strong losses, yet ones that could be difficult to discern in association with day *versus* nighttime sampling in the field because they fall within the temporal range of variability of INPs from nascent emissions over the course of a bloom. Events over the course of bloom 3 are noted in the timeline, using both panels to indicate all relevant natural changes or interventions. While nutrients were initially added to stimulate a natural phytoplankton bloom, the experiment was later spiked with a concentrated bloom that was produced by taking water from the channel and promoting a bloom in an external tank under natural sunlight. Peak Chl *a* ensued shortly after that spiking ("tank addition") of the bloom. Heterotrophic bacteria maximized about 4 days following peak Chl *a*, but also within a day of a needed cleaning of the wave flume walls to remove accumulated biofilms back into the flume water. Oxidation losses were thus greatest on three occasions: with the fresh seawater, following the tank addition and peak Chl *a*, and following wall cleaning and peak heterotrophic bacteria. Also emphasized in Fig. 5a is the fact that total INP concentrations were unchanged when sampling from the OFR without lamps powered on August 6.

The IS INP data timeline at 248 K (Fig. 5b) shows both similarities and differences with the CFDC timeline of nascent data and oxidation impacts. The dominant impact of the non-oxidative particle losses in the OFR for the particle size range that the IS filter captures is made clear by the proximity of the loss-corrected values to those found when the OFR was turned on. The single experiment on which these losses are based is indicated by the white-filled triangle on August 6 in Fig. 5b. Based on particle loss measurements (Fig. S4†), the IS filters should have collected particles up to at least 8 μm equivalent spherical diameter on the nascent line (6.5 μm larger than the CFDC cut-size), and up to 5 μm on the OFR, but with a 50% cut size for transmission at 3 μm. This defines the likely dominant size range for IS INPs as between about 2 and 8 μm, centered on the surface and volume modes of SSA. While confidence cannot be placed in the IS results for defining oxidation-induced changes in INPs in this size range, small but potentially significant decremental impacts of oxidation were noted through comparing OFR particle loss-corrected INPs and OFR measurements after the tank addition period. This period directly follows the OFR no-lamps experiment on August 6. The time of weakest oxidation impacts for particles assessed by the CFDC (July 29 to July 31; Fig. 5a) is indicated as a zero to slightly positive oxidation impact period for the corrected IS results (Fig. 5b). The most discrepant period of oxidation impacts in IS data is seen for the period at the beginning of the bloom experiment following fresh seawater addition, where large reductions are seen in the CFDC data and no or positive impacts in the IS results. We are not able to determine the reliability of these results.
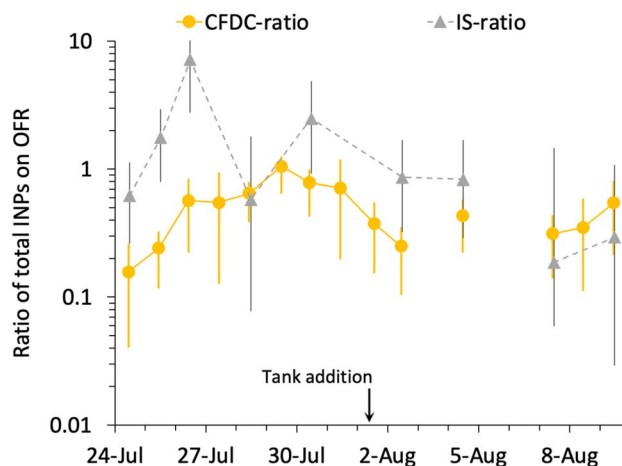

Fig. 6 Compilation of the ratio of INPs remaining following oxidation, computed as INPs through the OFR divided by INPs from nascent SSA sampling, with uncertainties added in quadrature. Uncertainties are much larger for the differencing method required to determine this ratio using the IS data corrected for OFR particle losses. Results, and these uncertainties may be grossly underestimated in this case.

Fig. 6 summarizes the timeline of ratios of OFR to nascent INP concentrations by both measurement methods. It is interesting that, excepting the 26th of July, the IS ratios trend with the CFDC ratios. Three of the 9 days of IS samples on and off the OFR show enhancements, but uncertainties are very large, such that only the 26th of July can be stated to above a ratio of 1 with significance ($p < 0.05$). However, it is interesting that the best agreement of IS and CFDC oxidative losses (measured for the CFDC, predicted for the IS) occurs in the few days after the physical loss test was performed (August 6). Clearly, this exercise could be improved through daily operation of the OFR with and without lights, but this was not practically possible during SeaSCAPE.

3.3 INP analytical results

On most days only one collection of INPs could be accommodated using the CFDC ice crystal impactor, and this was normally during the use of the aerosol concentrator (Fig. 2), to improve collection and identification statistics. In a few cases, substrate collections were also made for AFM or Raman analyses during the periods using the OFR when ice crystal residue number was much lower. No STEM samples were collected during the OFR periods.

3.3.1 Scanning transmission electron microscopy analyses of nascent INPs. Two dates of STEM collections were selected for analyses based on the timeline of results seen in Fig. 5. July 25 was a date of strong inferred oxidation impacts following the OFR, while July 30 was during the period of most limited OFR impacts on CFDC-measured INPs. For categorization of these data, we used composition and morphology, as documented by images shown in Fig. S9.† Categories were, (1) "core–shell" particles that possessed a dominant NaCl core, coatings of oxidized Mg, Ca and S salts, and inferred trace amounts of C, N, Si and K; (2) irregular particles of similar compositions but

© 2023 The Author(s). Published by the Royal Society of Chemistry

deficient or lacking in Cl; (3) round particles including small amounts of NaCl, Si and oxidized salts; (4) rod-like particles of more limited composition such as sulfates. Color-contrast imagery of elemental phases assisted this analysis, as shown in detail in Fig. S9.† For compositing purposes, we considered irregulars and rods together as an irregular category. It was difficult to determine the prism-like category identified in AFM categorizations (see Section 2.5.3). These could be part of the irregular and rod-like category in TEM data, but this was unclear.

Morphology pie charts and exemplary black and white images of these particles are shown for the two study dates in Fig. 7. The distinguishing factor between July 25 and July 30 was the proportion of all SSA INPs that were of the core–shell type dominating on July 25, while most INPs were of the irregular type on July 30. Absent images of INPs after the OFR, a general conclusion might be that the category most influenced by oxidation processes are particles with core–shell morphology, presented as large NaCl cores with surrounding salts and organic material.

3.3.2 Micro-Raman spectroscopy of re-activated nascent and aged INPs. Raman substrates were available for selected days during the phytoplankton bloom study, as listed in Table 1. An example of how these experiments were done is represented in Fig. 8. First, a dry Raman spectrum was recorded as shown in Fig. 8a ($T = 293$ K). This spectrum, with two peaks at 2900 and 2970 cm^{-1}, and minimal Raman peaks in other spectral regions, was identified. It is consistent with previous results for siliceous material which was detected as a major class of SSA[57] and SSA INPs[11] in a previous wave flume campaign. This is the predominant Raman spectral type attributed to diatomaceous cellular material. The relative humidity was then increased to drive condensation and formation of a microdroplet, as seen in Fig. 8b. The corresponding spectrum shows the appearance of a broad O–H Raman stretch centered around 3410 cm^{-1}, indicative of liquid water. Once a droplet formed, the temperature was decreased until freezing occurred, as seen in Fig. 8c; in this case freezing occurred at $T = 252$ K. This phase transition was accompanied by the characteristic spectral shift of the main Raman O–H stretching peak from 3410 to 3140 cm^{-1} and the appearance of two shoulders at 3255 and 3360 cm^{-1}, indicating the formation of ice.[47,58] This analysis was repeated on a single particle basis for over 50 particles.

Many of the same types of particles identified in McCluskey et al. (2018)[11] were also identified in SeaSCAPE analyses. These include three INP types that dominated INP residuals that refroze at temperatures >250 K. A first type was low signal particles assumed to be dominated by NaCl, which is Raman inactive. Trace organics could also be present, which could be the source for ice nucleation since NaCl freezes only ca. 225 K for 3–5 μm diameter droplets.[47,59] A second type was siliceous material, including other biologically-derived particles containing lipids (lipopolysaccharides and fatty alcohols), many similar to ones identified in McCluskey et al. (2018) to be active as INPs at 243 K.[11] Additionally, soot-like INP spectra were observed during SeaSCAPE. These results were determined
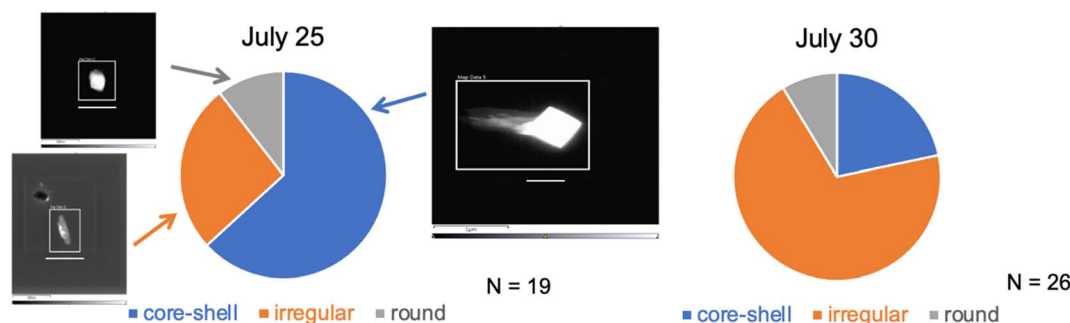

Fig. 7 Estimates of INP particle type proportions based on limited (numbers of particles analyzed are listed for each date) TEM analyses of nascent CFDC-collected INPs (on the two dates indicated). Three basic types are categorized based on details in the manuscript and ESI.† The white bars below each image are scaled at 1 μm.

Table 1 Ice nucleation onset temperatures for nascent and aged INPs isolated by the CFDC (with numbers of "first freezers" included in the onset measurements per sample indicated)

Date	Nascent ice nucleation onset temperature (K)	Aged ice nucleation onset temperature (K)
07-26-19	253.9 ± 2.3 ($N = 3$)	[a]
07-28-19	252.8 ± 1.0 ($N = 5$)	252 0.4 ± 1.3 ($N = 4$)
07-31-19	255.0 ± 1.6 ($N = 10$)	[a]
08-04-19	253.4 ± 4.5 ($N = 16$)	251.7 ± 2.2 ($N = 4$)
08-08-19	[a]	251.6 ± 1.2 ($N = 5$)
Average	253.8 ± 1.0	251.8 ± 0.2

[a] Indicates no substrate samples were collected from the CFDC.

© 2023 The Author(s). Published by the Royal Society of Chemistry

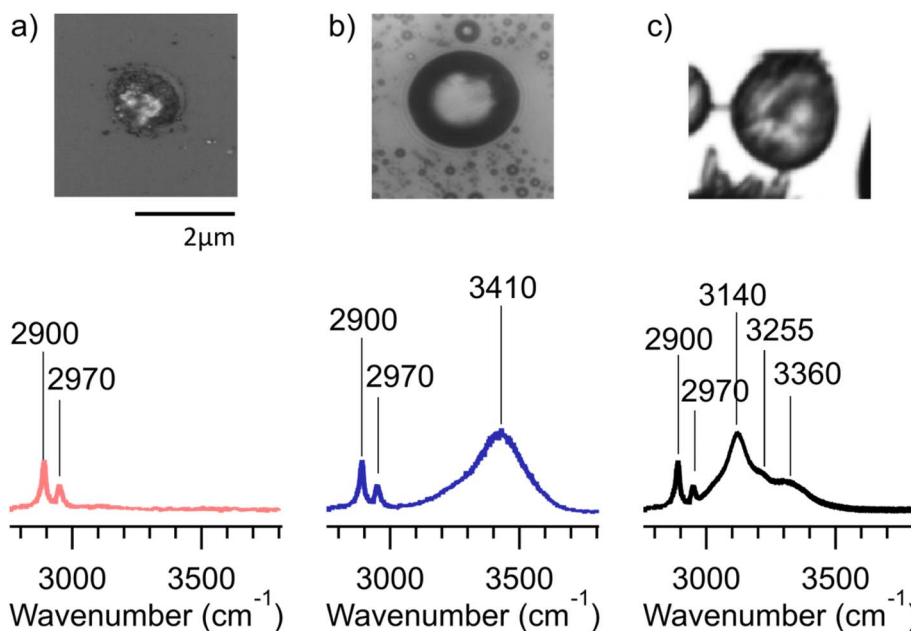Environ. Sci.: Atmos., 2023, **3**, 1513–1532 | **1523**

Fig. 8 Example images (top) and Raman spectra (bottom) of an approximately 1.5 μm-sized particle isolated through the CFDC and passed through the cold-stage water uptake and ice nucleation process. From the (a) initial dry particle (pink spectrum) through (b) wet particle (blue spectrum) following increased relative humidity and water droplet formation, and finally (c) frozen particle (black spectrum) after ice nucleation.
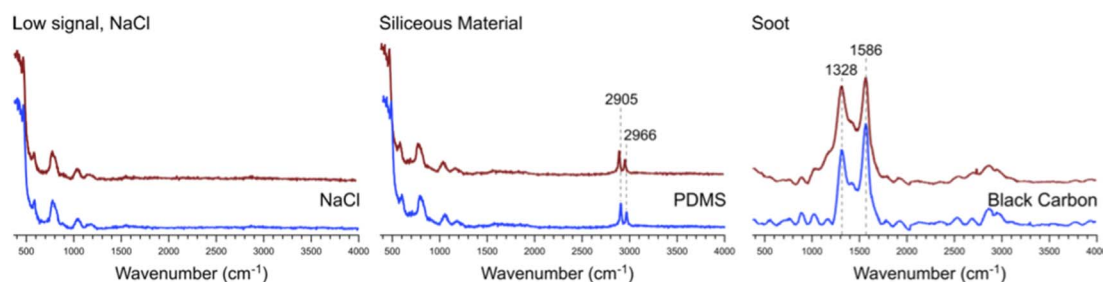

Fig. 9 Representative spectra #1, 2, and 3 from Fig. S10† (red) and the corresponding model system spectra (blue) for NaCl, PDMS, and black carbon to which these bear close similarity.

through comparison of INP residual spectra to model systems following Mael *et al.* (2021),[58] as documented in the ESI.† Results are shown in Fig. 9. While soot is used as the reference here, we note its similarity to the spectra of humic-like-substance (HULIS) spectra as reported by Deng *et al.* (2016).[60] Combustion soot is generally regarded as a very poor INP, and hence attribution in this case would be surprising.[61] The full set of common spectra are shown in Fig. S10 and S11,† while additional single spectra and further discussion can be found in Mael (2021).[62] Finally, it was observed that these dominant INP spectral types all froze over a range of temperatures >250 K, implying that factors other than composition (morphology, size) or secondary influence of unresolved organics could be important for freezing. The same was noted for more unique spectra active >250 K, such as two nearly identical INPs that had signatures of a long chain fatty acid and a similar fatty alcohol (Fig. S12†) and three that aligned with amino acids, L-trypto-phan, L-phenylalanine, and L-tyrosine (Fig. S13†).

Many other INPs with unique Raman spectra were found, especially for those refreezing below 250 K. These could not be identified through model systems or existing library compari-sons, although they could possibly be associated with biological species/components, pointing out again the rare nature and complex compositions of marine INPs that conspire to make them difficult to characterize. Due to many unidentified spectra, we do not attempt to state a partitioning of INP types as a function of temperature. Many different and unique INPs are emitted in SSA, dependent on water biology and chemistry, and these may not have unique freezing temperatures due to other factors, such as particle size. This makes specific attribution and parameterization based on composition quite difficult. Nevertheless, this study has added to a library of marine INPs for future identification. As an additional result from inspecting Raman spectra collected across all substrates (Fig. S10 and S11†), there was no obvious increase in oxygenation of the aged INPs compared to nascent INPs in the micrometer size range

analyzed by confocal Raman spectroscopy. This could be due to low signal and the relative insensitivity of Raman spectroscopy compared to other vibrational techniques or due to the loss of smaller, oxygenated species to the gas-phase.

The cold-stage micro-Raman data also provided insights into average ice nucleation onset freezing temperatures, which are reported for all nascent and aged INP collections for Raman analyses in Table 1. The particle density on each substrate collected from the CFDC ranged from 0–15 particles per 100 μm^2, this variation depending on the number of INPs activating at 243 K (nominal) in the CFDC at the given bloom stage, and the time available for collection. The ice nucleation onset temperatures reported for each date are based on 3 to 16 particles identified as first freezers per viewing area, accumulated over the entire substrate at the Raman cold-stage temperature set-points. We note again here that because these onset temperatures are much warmer than the CFDC operating temperature, not all subfields contained a particle that froze before the end temperature range of the environmental cell (246 K) was reached. Most interesting, as shown in Table 1, is a suppression in ice nucleation onset temperature by *ca.* 2 K in the particles that were aged in the PAM-OFR. For nascent SSA INPs typically a 2× increase in INP concentration per 1 K cooling is observed. Thus, a 2 K temperature suppression measured in the cold-stage micro-Raman experiments is roughly comparable to a 4× reduction in INP

concentration at a given temperature. While data are limited, this change agrees reasonably well with the noted 2–5 times reductions in INP concentrations occurring for aged INPs in CFDC and IS measurements. Additionally, this small change in ice nucleation onset temperature agrees with earlier studies of the impacts of aging on freezing of organic and biological particles with oxidants and atmospheric gases (ozone and nitric acid).[46,63]

3.3.3 Relative distribution of morphologies of nascent and aged INPs *via* AFM. Fig. 10a shows representative AFM 3D-height images of five main morphologies observed for nascent and aged INPs. For each sample type, the characterized particles were within the volume-equivalent diameter range of 0.1–1.0 μm. Morphological categorization was performed qualitatively as described previously.[49,50,53,64,65] Nascent INPs displayed five unique morphologies including: prism-like, core–shell, rounded, aggregate, and core–shell with inclusion, while INPs following oxidation had only core–shell, prism-like, and aggregate morphologies for particles assessed.

Fig. 10b shows an average with one standard deviation for the fraction of particles from each morphological category for both INP and INP-OFR samples. For each sample type, core–shell was the most abundant, followed by prism-like. Compared to nascent INPs, INP-OFR (aged INPs) had a higher abundance of core–shell (∼40% *versus* ∼66%), and a significant reduction of rounded (∼8% *versus* ∼0%) and core–shell with inclusion
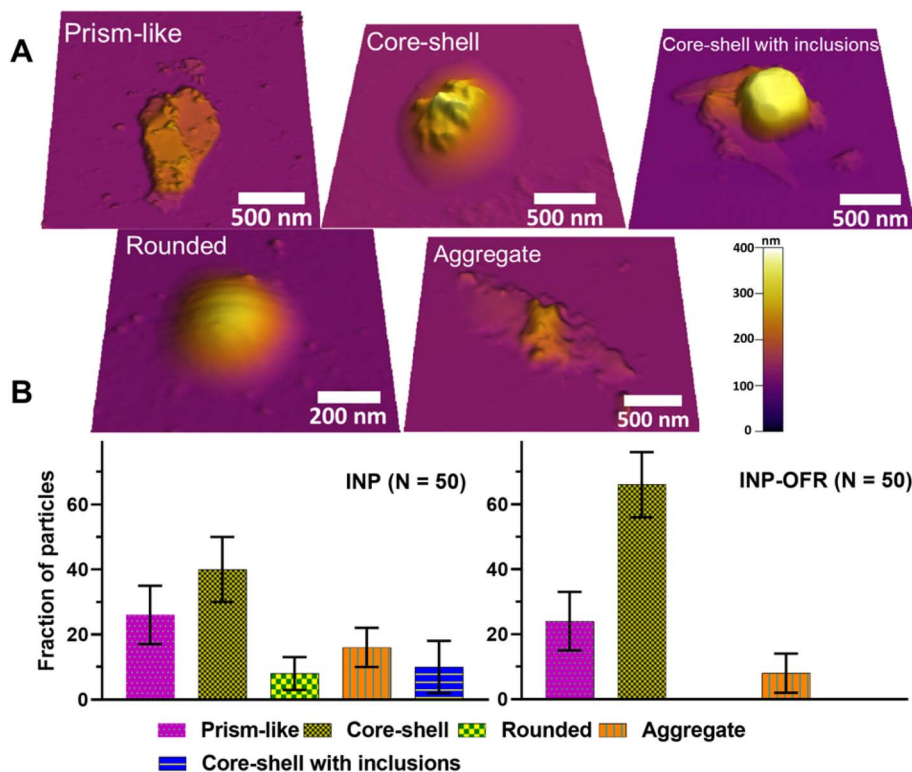

Fig. 10 (a) Selected illustrative AFM 3D-height images of five main morphological categories (prism-like, core−shell, rounded, aggregate, and core−shell with inclusions) identified for both INP and INP-OFR samples. The maximum height range is 400 nm for each image. (b) Fraction of particles (%) from each morphological category between INP and INP-OFR samples. For each sample type, the characterized individual particles (*N* = 50 for each sample) had similar volume-equivalent diameter range of 0.1–1.0 μm.

(~10% *versus* ~0%) particles. The statistical probability distribution analysis (Fig. S14†) was utilized to assess the relative distribution of each morphology type for a theoretical population of 10 000 particles from nascent and aged INP populations. Based on this analysis, we establish a statistically significant difference in the relative abundance for core–shell morphology. Specifically, for both INP and INP-OFR categories, the probability of obtaining core–shell particles was significantly higher than for other morphologies. Furthermore, the fraction of core–shell particles under oxidation (INP-OFR) was larger and significantly different from the nascent INPs. That is, the observed increase in the relative abundance of core–shell morphology in the INP-OFR population is a statistically significant observation despite the finite number of individual particles studied here for each sample.

These findings may, as a corollary, suggest a significant reduction of ice nucleating ability for rounded and core–shell with inclusion particles following heterogeneous oxidation, or they may simply reflect that the proportion of core–shell particles is greater following oxidation impacts on all INP types. There are a few explanations for this result. First, heterogeneous oxidation can change the viscosity of organic matter in particles,[66] which in turn could facilitate phase segregation of organic and inorganic components within the particle, leading to the formation of more core–shell particles inside the PAM-OFR.[28] Second, and alternately, gas phase molecules produced during the heterogeneous oxidation[17] could condense onto the particle surface resulting in formation of more core–shell sea spray particles in the PAM-OFR.[28] Either process is consistent with the limited TEM analyses which suggested oxidation impacts were stronger when core–shell particles were the

Fig. 11 Relative distributions of the solid, semisolid, and liquid phase states at 20% and 60% RH_w for the shell region of core–shell INP (panel A) and INP-OFR (panel B). For each sample, the characterized individual particles ($N = 11$ for INP, and $N = 30$ for INP-OFR) had a similar volume-equivalent diameter range of 0.1–1.0 μm.

Table 2 Summary of sample type for core–shell particles, the average with one standard deviation of fraction of particles with solid, semisolid, and liquid shells at 20% and 60% RH_w, and viscoelastic response distance (VRD) and VRD range for the semisolid shells

Sample type	RH_w	Solid (%)	Semisolid (%)	Liquid (%)	VRD (nm)	VRD range (nm)
INP	20%	45 ± 20	55 ± 24	0	2.4 ± 1.8	0.8–5.5
	60%	27 ± 9	73 ± 22	0	3.6 ± 2.4	1.0–6.8
INP-OFR	20%	17 ± 9	83 ± 11	0	3.6 ± 2.2	1.1–10.3
	60%	7 ± 3	89 ± 10	4 ± 1	5.0 ± 5.9	0.8–29.0

dominant nascent INPs types. The TEM results do not support that the balance toward core–shell types following oxidation was created by a stronger loss of other types (rounded and inclusion types). Future studies using model aerosol systems should be carried out to better understand these loss processes.

Fig. 11 and Table 2 show the relative distribution of phase states for the shell region of core–shell particles from INP and INP-OFR samples, at 20% and 60% RH$_w$. A total of 11 and 30 individual core–shell particles were studied for nascent and aged samples, respectively. A statistical probability distribution analysis was also utilized to assess the relative distribution of solid and semisolid phase states between the two sample types (Fig. S15†). At 20% RH$_w$, nascent INPs showed an approximately even relative abundance of solid and semisolid shells, and as RH$_w$ increased to 60%, the relative abundance of semisolid shells increased. In contrast, core–shell aged INPs primarily had semisolid shells at 20% RH$_w$, and as RH$_w$ increased to 60%, the majority of shells remained semisolid, while ~4% of the shells turned into liquid. Additionally, at both RH$_w$ values, the nascent INPs had the highest abundance of core-shells with solid shells in comparison to aged INPs. The VRD values collected on semisolid shells of core–shell particles from INPs and INP-OFR are listed in Table 2. Briefly, the VRD values measured on aged INP shells are noticeably higher than those of the nascent INPs, which is likely indicative of lowered shell viscosity following heterogeneous oxidation. Previous study has shown that heterogeneous oxidation generally leads to the formation of more soluble and oxygenated products,[66] and hence the increased abundance of semisolid shells with likely lower viscosity in INP-OFR particles could be due to the presence of more oxygenated chemical species in the shells of core–shell particles. Recent studies of the effects of atmospheric aging processes on nascent SSA core–shell morphologies showed that aging resulted in the formation of more water soluble and oxygenated shells.[67] Nevertheless, we note that this result appears to be inconsistent with conclusions based on the Raman spectra, which showed no apparent difference in oxygenation between aged and nascent INPs. This difference could be due to size effects as the AFM analyses were conducted on submicron sized particles, whereas the Raman analyses were on larger supermicron sized particles. More likely, as discussed above, the relative insensitivity of Raman spectroscopy to detect these changes in oxygenation may be the reason for this difference.

The phase state of the other main morphologies at 20% and 60% RH$_w$ were investigated by probing at the approximate center of prism-like and rounded particles, and at the shell and inclusion regions for core–shell with inclusion particles. Prism-like particles from the INP and INP-OFR samples were predominantly solid at 20% RH$_w$ and showed an approximately even relative abundance of solid and semisolid phase states at 60% RH$_w$. At both 20% and 60% RH$_w$, rounded INPs were primarily solid, while core–shell with inclusion INP had semi-solid shells and solid inclusions. Note, larger VRD values observed for the semisolid aged INPs relative to semisolid nascent INPs likely indicates lower viscosity of the shells as a result of aging, which suggests formation of more soluble

shells, consistent with our previous studies on nascent and aged SSA.[67]

4. Conclusion

INP concentrations from nascent SSA from wave-breaking in a laboratory wave flume and following exposure of the same particles to OH radicals in an OFR to simulate atmospheric aging over periods of 3 to 8 days, indicated losses of INPs (degradation of INP number concentrations) in the range of 2 to 5 times were found. These losses over atmospherically relevant time scales occurred for INPs active over a range of temperatures down to at least 243 K. These oxidative losses based on online INP measurements could not be confirmed with confidence through offline immersion freezing measurements using collected filters because of strong losses of supermicron particles in the OFR, and so the need remains to explore the role of oxidation processes on supermicron mode INPs. As a secondary result of particle losses in the OFR, these studies confirm the expected dominance of supermicron SSA INP emissions found to emanate from jet drop emissions. Nevertheless, through measurements of INPs collected in real-time from a CFDC operating at ~243 K, and then re-activated in a cold-stage Raman system at temperatures as high as 263 K, a depression in freezing onset equivalent to ~2 K was identified for aged SSA INPs in the sub-1.5 μm dry aerodynamic size range. This aligns with the 2–5 times losses measured in the CFDC, in consideration of previously measured temperature dependence of SSA INP concentrations at >243 K.[11] We may note that this degradation in ice nucleation activity for organic SSA INPs under oxidation is comparable to results previously reported for freshwater dissolved organic matter acting as INPs.[23] The magnitude of these oxidation losses may be dwarfed by the spread in INP concentrations found in atmospheric studies over oceans and elsewhere but may be at the root of some of the measured atmospheric variability, and nevertheless represent the first such measurements.[8,9,68] This deserves more laboratory and field study, for example in high latitude regions where polar night eliminates many oxidation processes.

Through combining enhanced collection of activated INPs with a variety of analytical techniques, new insights were gained into INP compositions and on which subtypes are most impacted by oxidation processes. While analytical studies of INPs collected at ~243 K could not establish if one or more types of INPs are compromised by heterogeneous oxidation in a detrimental way, overall highest impact was particularly associated with days when the largest proportion of INPs were those that contained NaCl cores with inorganic salts and organic carbon surrounding them, which was most oftentimes the major aerosol type. On a day with especially strong oxidation impacts on sub-1.5 μm aerodynamic diameter (spherical-equivalent, dry size) particles measured by the CFDC, STEM/EDX analyses showed a dominance of this INP type from nascent SSA. On a day without observable oxidation impacts, likely due to the biochemical state of the water and its surface microlayer during the mesocosm-induced bloom, nascent INPs were dominated by irregular particles without a dominant

© 2023 The Author(s). Published by the Royal Society of Chemistry

Environ. Sci.: Atmos., 2023, **3**, 1513–1532 | 1527

STEM/EDX salt signature. AFM analyses contrasting the morphologies of nascent and aged INPs indicated statistically significant increases in the relative abundance of core–shell morphology INPs following oxidation, but these particles were also shown to have transitioned to more semi-solid phase states that may not favor ice nucleation. The loss or lower abundance of round and irregular INPs following aging in AFM results may appear in contradiction to STEM analyses indicating that these types dominated nascent INPs on days without oxidation impacts. However, it must be recalled that these are proportional analyses. No STEM collections were made for aged particles due to an emphasis on sharing those collection times for Raman and AFM analyses. We conclude that it is the prevalence of core–shell INPs in the first place that is most associated with oxidation–induced reduction of INP concentrations.

Based on AFM analyses of INP phase states before and after oxidation, it might be inferred that the observed reduction in INP concentrations due to heterogeneous oxidation could be related to the increase of core–shell particles with semisolid shells (at both 20% and 60% RH$_w$) and likely lower viscosity in INP-OFR sample, compared to the INP sample where more solid shells (with likely higher viscosity) were observed. Whether the responsible oxidation impacts occur on the original organic shells or *via* condensation of material from the gas phase cannot be discerned. Further, changes in organic functionalization could not be discerned in Raman studies, as no discernible changes in oxidation states were observed between nascent and aged INPs. As well, how any change in particle functionalization and phase state translates to impacts on immersion freezing in more dilute condensed water within activated cloud droplets (as in the CFDC) remains to be understood in future studies.

The most novel and challenging studies used the enhanced collection of particles activated in real-time at 243 K which were reactivated across a range of temperatures using the cold-stage micro-Raman device to focus on compositional types of INPs. Despite these efforts, results confirmed that INP compositions in SSA remain difficult to describe in a simplistic manner. While some similar types of INPs were found in this study as in prior wave flume studies that were focused only at 243 K, such as siliceous material and fatty acids or alcohols, a wide range of other entities were identified that included soot (or HULIS), amino acids, hydrates and aliphatics. These have greatly augmented Raman spectral libraries of SSA INPs. Nevertheless, it was not possible to attribute proportions of INP types quantitatively as a function of temperature because of a preponderance of INP spectral compositions that were low signal (likely NaCl) or unidentified. Results also confirmed that even individual compositions do not necessarily always have unique freezing temperatures, possibly indicating the role of other factors such as size, morphology and interactions with inorganic content.

The results of this study promote future experiments that can explore oxidative impacts on the full SSA particle size distribution. When extending studies to temperatures of most relevance to mixed-phase clouds, which we attempted here *via* concentration of collected INPs, experiments may always involve size biases when employing OFR instruments, unless special modifications are made to ameliorate particle losses. Studies employing smog chambers could be explored for learning more about the typical degradation of INP efficiency that occurs under oxidation by OH radicals. Other spectral methods, including single particle TOF mass spectrometry, may ultimately assist the effort to relate these INP changes to aerosol composition changes. Finally, these measurements also promote the need for insightful atmospheric measurements using an OFR or smog chambers and using varied solar cycles to gain understanding of the role of oxidation following emission of SSA INPs over remote ocean regions. Such data do not presently exist from field measurements.

Author contributions

Conflicts of interest

There are no conflicts to declare.

Acknowledgements

References

1 U. Dusek, G. P. Frank, L. Hildebrandt, J. Curtius, J. Schneider, S. Walter, D. Chand, F. Drewnick, S. Hings, D. Jung, S. Borrmann and M. O. Andreae, Size Matters More Than Chemistry for Cloud-Nucleating Ability of Aerosol Particles, *Science*, 2006, **312**(5778), 1375–1378, DOI: **10.1126/science.1125261**.

2 B. Ervens, M. J. Cubison, E. Andrews, G. Feingold, J. A. Ogren, J. L. Jimenez, P. K. Quinn, T. S. Bates, J. Wang, Q. Zhang, H. Coe, M. Flynn and J. D. Allan, CCN predictions using simplified assumptions of organic aerosol composition and mixing state: a synthesis from six different locations, *Atmos. Chem. Phys.*, 2010, (10), 4795–4807, DOI: **10.5194/acp-10-4795-2010**.

3 D. B. Collins, T. H. Bertram, C. M. Sultana, C. Lee, J. L. Axson and K. A. Prather, Phytoplankton blooms weakly influence the cloud forming ability of sea spray aerosol, *Geophys. Res. Lett.*, 2016, **43**, 9975–9983, DOI: **10.1002/2016GL069922**.

4 H. C. Che, X. Y. Zhang, L. Zhang, Y. Q. Wang, Y. M. Zhang, X. J. Shen, Q. L. Ma, J. Y. Sun and J. T. Xhong, Prediction of size-resolved number concentration of cloud condensation nuclei and long-term measurements of their activation characteristics, *Sci. Rep.*, 2017, **7**, 5819, DOI: **10.1038/s41598-017-05998-3**.

5 Z. A. Kanji, L. A. Ladino, H. Wex, Y. Boose, M. Burkert-Kohn, D. J. Cziczo and M. Krämer, Overview of ice nucleating particles, *Meteorol. Monogr.*, 2017, **58**, 1.1–1.33, DOI: **10.1175/AMSMONOGRAPHS-D-16-0006.1**.

6 P. J. DeMott, T. C. J. Hill, C. S. McCluskey, K. A. Prather, D. B. Collins, R. C. Sullivan, M. J. Ruppel, R. H. Mason, V. E. Irish, T. Lee, C. Y. Hwang, T. S. Rhee, J. R. Snider, G. R. McMeeking, S. Dhaniyala, E. R. Lewis, J. J. B. Wentzell, J. Abbatt, C. Lee, C. M. Sultana, A. P. Ault, J. L. Axson, M. Diaz Martinez, I. Venero, G. Santos-Figueroa, M. D. Stokes, G. B. Deane, O. L. Mayol-Bracero, V. H. Grassian, T. H. Bertram, A. K. Bertram, B. F. Moffett and G. D. Franc, Sea spray aerosol as a unique source of ice nucleating particles, *Proc. Natl. Acad. Sci. U. S. A.*, 2016, **113**(21), 5797–5803, DOI: **10.1073/pnas.1514034112**.

7 C. S. McCluskey, J. Ovadnevaite, M. Rinaldi, J. Atkinson, F. Belosi, D. Ceburnis, S. Marullo, T. C. J. Hill, U. Lohmann, Z. A. Kanji, C. O'Dowd, S. M. Kreidenweis and P. J. DeMott, Marine and Terrestrial Organic Ice Nucleating Particles in Pristine Marine to Continentally-Influenced Northeast Atlantic Air Masses, *J. Geophys. Res.: Atmos.*, 2018, **123**, 6196–6212, DOI: **10.1029/2017JD028033**.

8 C. S. McCluskey, P. J. DeMott, P.-L. Ma and S. M. Burrows, Numerical representations of marine ice-nucleating particles in remote marine environments evaluated against observations, *Geophys. Res. Lett.*, 2019, **46**, 7838–7847, DOI: **10.1029/2018GL081861**.

9 X. Zhao, X. Liu, S. M. Burrows and Y. Shi, Effects of marine organic aerosols as sources of immersion-mode ice-nucleating particles on high-latitude mixed-phase clouds, *Atmos. Chem. Phys.*, 2021, **21**, 2305–2327, DOI: **10.5194/acp-21-2305-2021**.

10 S. M. Burrows, S. C. Hoose, U. Pöschl and M. G. Lawrence, Ice nuclei in marine air: Biogenic particles or dust?, *Atmos. Chem. Phys.*, 2013, **13**(1), 245–267, DOI: **10.5194/acp-22-847-2022**.

11 C. S. McCluskey, T. C. J. Hill, C. M. Sultana, O. Laskina, J. Trueblood, M. V. Santander, C. M. Beall, J. M. Michaud, S. M Kreidenweis, K. A. Prather, V. H. Grassian and P. J. DeMott, A mesocosm double feature: Insights into the chemical make-up of marine ice nucleating particles, *J. Atmos. Sci.*, 2018, **75**, 2405–2423, DOI: **10.1175/JAS-D-17-0155.1**.

12 I. Steinke, P. J. DeMott, G. B. Deane, T. C. J. Hill, M. Maltrud, A. Raman and S. M. Burrows, A numerical framework for simulating the atmospheric variability of supermicron marine biogenic ice nucleating particles, *Atmos. Chem. Phys.*, 2022, **22**, 847–859, DOI: **10.5194/acp-22-847-2022**.

13 P. A. Alpert, J. Y. Aller and D. A. Knopf, Initiation of the ice phase by marine biogenic surfaces in supersaturated gas and supercooled aqueous phases, *Phys. Chem. Chem. Phys.*, 2011, **13**, 19882–19894, DOI: **10.1039/C1CP21844A**.

14 R. J. Perkins, M. G. Vazquez de Vasquez, E. E. Beasely, E. A. Stone, H. C. Allen and P. J. DeMott, Relating Structure and Ice Nucleation of Mixed Surfactant Systems Relevant to Sea Spray Aerosol, *J. Phys. Chem. A*, 2020, **124**(42), 8806–8821, DOI: **10.1021/acs.jpca.0c0584910.1021/acs.jpca.0c05849**.

15 P. A. Alpert, W. P. Kilthau, R. E. O'Brien, R. C. Moffet, M. K. Gilles, B. Wang, A. Laskin, J. Y. Aller and D. A. Knopf, Ice-nucleating agents in sea spray aerosol identified and quantified with a holistic multimodal freezing model, *Sci. Adv.*, 2022, **8**(44), 11, DOI: **10.1126/sciadv.abq6842**.

16 I. George and J. Abbatt, Heterogeneous oxidation of atmospheric aerosol particles by gas-phase radicals, *Nat. Chem.*, 2010, **2**, 713–722, DOI: **10.1038/nchem.806**.

17 J. H. Kroll, C. Y. Lim, S. H. Kessler and K. R. Wilson, Heterogeneous Oxidation of Atmospheric Organic Aerosol: Kinetics of Changes to the Amount and Oxidation State of Particle-Phase Organic Carbon, *J. Phys. Chem. A*, 2015, **119**(44), 10767–10783, DOI: **10.1021/acs.jpca.5b06946**.

18 M. Rinaldi, S. Decesari, E. Finessi, L. Giulianelli, C. Carbone, S. Fuzzi, C. D. O'Dowd, D. Ceburnis and M. C. Facchini, Primary and Secondary Organic Marine Aerosol and Oceanic Biological Activity: Recent Results and New Perspectives for Future Studies, *Adv. Meteorol.*, 2010, **2010**, 310682, DOI: **10.1155/2010/310682**.

19 A. D. Estillore, J. V. Trueblood and V. H. Grassian, Atmospheric chemistry of bioaerosols: heterogeneous and multiphase reactions with atmospheric oxidants and other trace gases, *Chem. Sci.*, 2016, **7**, 6604–6616, DOI: **10.1039/c6sc02353c**.

20 J. V. Trueblood, X. Wang, V. W. Or, M. R. Alves, M. V. Santander, K. A. Prather and V. H. Grassian, The Old and the New: Aging of Sea Spray Aerosol and Formation of Secondary Marine Aerosol through OH Oxidation

© 2023 The Author(s). Published by the Royal Society of Chemistry

Environ. Sci.: Atmos., 2023, **3**, 1513–1532 | **1529**

Reactions, *ACS Earth Space Chem.*, 2019, **3**(10), 2307–2314, DOI: 10.1021/acsearthspacechem.9b00087.

21 K. J. Mayer, X. Wang, M. V. Santander, B. A. Mitts, J. S. Sauer, C. M. Sultana, C. D. Cappa and K. A. Prather, Secondary Marine Aerosol Plays a Dominant Role over Primary Sea Spray Aerosol in Cloud Formation, *ACS Cent. Sci.*, 2020, **6**(12), 2259–2266, DOI: 10.1021/acscentsci.0c00793.

22 R. S. Humphries, M. D. Keywood, S. Gribben, I. M. McRobert, J. P. Ward, P. Selleck, S. Taylor, J. Harnwell, C. Flynn, G. R. Kulkarni, G. G. Mace, A. Protat, S. P. Alexander and G. McFarquhar, Southern Ocean latitudinal gradients of cloud condensation nuclei, *Atmos. Chem. Phys.*, 2021, **21**, 12757–12782, DOI: 10.5194/acp-21-12757-2021.

23 N. Borduas-Dedekind, R. Ossola, R. O. David, L. S. Boynton, V. Weichlinger, A. A. Kanji and K. McNeill, Photomineralization mechanism changes the ability of dissolved organic matter to activate cloud droplets and to nucleate ice crystals, *Atmos. Chem. Phys.*, 2019, **19**, 12397–12412, DOI: 10.5194/acp-19-12397-2019.

24 S. J. Biller, F. Schubotz, S. E. Roggensack, A. W. Thompson, R. E. Summons and S. W. Chisholm, Bacterial Vesicles in Marine Ecosystems, *Science*, 2014, **343**(6167), 183–186, DOI: 10.1126/science.1243457.

25 P. Verdugo, *Marine Microgels*, 2012, **4**(1), 375–400, DOI: 10.1146/annurev-marine-120709-142759.

26 D. A. Knopf, P. A. Alpert and B. Wang, *ACS Earth Space Chem.*, 2018, **2**(3), 168–202, DOI: 10.1021/acsearthspacechem.7b00120.

27 S. Kasparoglu, R. Perkins, P. J. Ziemann, P. J. DeMott, S. M. Kreidenweis, Z. Finewax, B. L. Deming, M. P. DeVault and M. D. Petter, Experimental determination of the relationship between organic aerosol viscosity and ice nucleation at upper free tropospheric conditions, *J. Geophys. Res.: Atmos.*, 2022, **127**, e2021JD036296, DOI: 10.1029/2021JD036296.

28 J. S. Sauer, K. J. Mayer, C. Lee, M. R. Alves, S. Amiri, C. J. Bahaveolos, E. B. Franklin, D. R. Crocker, D. Dang, J. Dinasquet, L. A. Garofalo, C. P. Kaluarachchi, D. B. Kilgour, L. Mael, B. A. Mitts, D. R. Moon, A. N. Moore, C. K. Morris, C. A. Mullenmeister, C.-M. Ni, M. A. Pendergraft, D. Petras, R. M. C. Simpson, S. Smith, P. R. Tumminello, J. L. Walker, P. J. DeMott, D. K. Farmer, A. H. Goldstein, V. H. Grassian, J. S. Jaffe, F. Malfatti, T. R. Martz, J. H. Slade, A. V. Tivanski, T. H. Bertram, C. D. Cappa and K. A. Prather, The Sea Spray Chemistry and Particle Evolution study (SeaSCAPE): overview and experimental methods, *Environ. Sci.: Processes Impacts*, 2022, **24**, 290–315, DOI: 10.1039/D1EM00260K.

29 K. A. Prather, T. H. Bertram, V. H. Grassian, G. B. Deane, M. D. Stokes, P. J. DeMott, L. I. Aluwihare, B. Palenik, F. Azam, J. H. Seinfeld, R. C. Moffet, M. J. Molina, C. D. Cappa, F. M. Geiger, G. C. Roberts, L. M. Russell, A. P. Ault, J. Baltrusaitis, D. B. Collins, C. E. Corrigan, L. A. Cuadra-Rodriguez, C. J. Ebben, S. D. Forestieri, T. L. Guasco, S. P. Hersey, M. J. Kim, W. Lambert, R. L. Modini, W. Mui, B. E. Pedler, M. J. Ruppel,

O. S. Ryder, N. Schoepp, R. C. Sullivan and D. Zhao, Bringing the ocean into the laboratory to probe the chemical complexity of sea spray aerosol, *Proc. Natl. Acad. Sci. U. S. A.*, 2013, **110**(19), 7550–7555, DOI: 10.1073/pnas.1300262110.

30 X. Wang, C. M. Beall, C. S. McCluskey, G. C. Cornwell, Y. Zhou, J. L. Cox, M. A. Pendergraft, M. V. Santander, T. H. Bertram, C. D. Cappa, F. Azam, P. J. DeMott, V. H. Grassian and K. A. Prather, Microbial control of sea spray aerosol composition: A tale of two blooms, *ACS Cent. Sci.*, 2015, **1**, 124–131, DOI: 10.1021/acscentsci.5b00148.

31 P. J. DeMott, A. J. Prenni, G. R. McMeeking, Y. Tobo, R. C. Sullivan, M. D. Petters, M. Niemand, O. Möhler and S. M. Kreidenweis, Integrating laboratory and field data to quantify the immersion freezing ice nucleation activity of mineral dust particles, *Atmos. Chem. Phys.*, 2015, **15**, 393–409, DOI: 10.5194/acp-15-393-2015.

32 K. R. Barry, T. C. J. Hill, E. J. T. Levin, C. H. Twohy, K. A. Moore, Z. D. Weller, D. W. Toohey, M. Reeves, T. Campos, R. Geiss, E. V. Fischer, S. M. Kreidenweis and P. J. DeMott, Observations of ice nucleating particles in the free troposphere from western US wildfires, *J. Geophys. Res.: Atmos.*, 2021, **126**, e2020JD033752, DOI: 10.1029/2020JD033752.

33 P. J. DeMott, T. C. J. Hill, M. D. Petters, A. K. Bertram, Y. Tobo, R. H. Mason, K. J. Suski, C. S. McCluskey, E. J. T. Levin, G. P. Schill, Y. Boose, A. M. Rauker, A. J. Miller, J. Zaragoza, K. Rocci, N. E. Rothfuss, H. P. Taylor, J. D. Hader, C. Chou, J. A. Huffman, U. Pöschl, A. J. Prenni and S. M. Kreidenweis, Comparative measurements of ambient atmospheric concentrations of ice nucleating particles using multiple immersion freezing methods and a continuous flow diffusion chamber, *Atmos. Chem. Phys.*, 2017, **17**, 11227–11245, DOI: 10.5194/acp-17-11227-2017.

34 P. J. DeMott, O. Möhler, D. J. Cziczo, N. Hiranuma, M. D. Petters, S. S. Petters, F. Belosi, H. G. Bingemer, S. D. Brooks, C. Budke, M. Burkert-Kohn, K. N. Collier, A. Danielczok, O. Eppers, L. Felgitsch, S. Garimella, H. Grothe, P. Herenz, T. C. J. Hill, K. Höhler, Z. A. Kanji, A. Kiselev, T. Koop, T. B. Kristensen, K. Krüger, G. Kulkarni, E. J. T. Levin, B. J. Murray, A. Nicosia, D. O'Sullivan, A. Peckhaus, M. J. Polen, H. C. Price, N. Reicher, D. A. Rothenberg, Y. Rudich, G. Santachiara, T. Schiebel, J. Schrod, T. M. Seifried, F. Stratmann, R. C. Sullivan, K. J. Suski, M. Szakáll, H. P. Taylor, R. Ullrich, J. Vergara-Temprado, R. Wagner, T. F. Whale, D. Weber, A. Welti, T. W. Wilson, M. J. Wolf and J. Zenker, The Fifth International Workshop on Ice Nucleation phase 2 (FIN-02): laboratory intercomparison of ice nucleation measurements, *Atmos. Meas. Tech.*, 2018, **11**, 6231–6257, DOI: 10.5194/amt-11-6231-2018.

35 C. S. McCluskey, P. J. DeMott, A. J. Prenni, E. J. T. Levin, G. R. McMeeking, A. P. Sullivan, T. C. J. Hill, S. Nakao, C. M. Carrico and S. M. Kreidenweis, Characteristics of atmospheric ice nucleating particles associated with biomass burning in the US: Prescribed burns and

wildfires, *J. Geophys. Res.: Atmos.*, 2014, **119**, 10458–10470, DOI: **10.1002/2014JD021980**.

36 C. S. McCluskey, T. C. J. Hill, F. Malfatti, C. M. Sultana, C. Lee, M. V. Santander, C. M. Beall, K. A. Moore, G. C. Cornwell, D. B. Collins, K. A. Prather, K. Jayarathne, E. Stone, F. Azam, S. M. Kreidenweis and P. J. DeMott, A dynamic link between ice nucleating particles released in nascent sea spray aerosol and oceanic biological activity during two mesocosm experiments, *J. Atmos. Sci.*, 2017, **74**, 151–166, DOI: **10.1175/JAS-D-16-0087.1**.

37 F. J. Romay, D. L. Roberts, V. A. Marple, B. Y. H. Liu and B. A. Olson, A High-Performance Aerosol Concentrator for Biological Agent Detection, *Aerosol Sci. Technol.*, 2002, **36**(2), 217–226, DOI: **10.1080/027868202753504074**.

38 Y. Tobo, A. J. Prenni, P. J. DeMott, J. A. Huffman, C. S. McCluskey, G. Tian, C. Pöhlker, U. Pöschl and S. M. Kreidenweis, Biological aerosol particles as a key determinant of ice nuclei populations in a forest ecosystem, *J. Geophys. Res.: Atmos.*, 2013, **118**, 10100–10110, DOI: **10.1002/jgrd.50801**.

39 E. J. T. Levin, G. R. McMeeking, P. J. DeMott, C. S. McCluskey, C. M. Carrico, S. Nakao, C. E. Stockwell, R. J. Yokelson and S. M. Kreidenweis, Ice-nucleating particle emissions from biomass combustion and the potential importance of soot aerosol, *J. Geophys. Res.: Atmos.*, 2016, **121**(10), 5888–5903, DOI: **10.1002/2016JD024879**.

40 D. C. Rogers, P. J. DeMott, S. M. Kreidenweis and Y. Chen, Measurements of ice nucleating aerosols during SUCCESS, *Geophys. Res. Lett.*, 1998, (25), 1383–1386, DOI: **10.1029/97GL03478**.

41 M. D. Petters and S. M. Kreidenweis, A single parameter representation of hygroscopic growth and CCN activity, *Atmos. Chem. Phys.*, 2007, 7, 1961–1971, DOI: **10.5194/acp-7-1961-2007**.

42 G. Vali, Quantitative Evaluation of Experimental Results and the Heterogeneous Freezing Nucleation of Supercooled Liquids, *J. Atmos. Sci.*, 1971, **28**, 402, DOI: **10.1175/1520-0469(1971)028<0402:QEOERA>2.0.CO;2**.

43 A. Agresti and B. A. Coull, Approximate is better than "exact" for interval estimation of binomial proportions, *Am. Stat.*, 1998, **52**, 119–126, DOI: **10.2307/2685469**.

44 M. D. Stokes, G. B. Deane, K. A. Prather, T. H. Bertram, M. J. Ruppel, O. S. Ryder, J. M. Brady and D. Zhao, A Marine Aerosol Reference Tank system as a breaking wave analogue for the production of foam and sea-spray aerosols, *Atmos. Meas. Tech.*, 2013, **6**, 1085–1094, DOI: **10.5194/amt-6-1085-2013**.

45 B. A. Mitts, X. Wang, D. D. Lucero, C. M. Beall, G. B. Deane, P. J. DeMott and K. A. Prather, Importance of supermicron ice nucleating particles in nascent sea spray, *Geophys. Res. Lett.*, 2021, **48**, e2020GL089633, DOI: **10.1029/2020GL089633**.

46 L. E. Mael, H. Busse and V. H. Grassian, Measurements of Immersion Freezing and Heterogeneous Chemistry of Atmospherically Relevant Single Particles with Micro-Raman Spectroscopy, *Anal. Chem.*, 2019, **91**, 11138–11145, DOI: **10.1021/acs.analchem.9b01819**.

47 L. E. Mael, G. Peiker, H. Busse and V. H. Grassian, Temperature-Dependent Liquid Water Structure for Individual Micron-Sized, Supercooled Aqueous Droplets with Inclusions, *J. Phys. Chem. A*, 2021, **125**(51), 10742–10749, DOI: **10.1021/acs.jpca.1c08331**.

48 C. P. Kaluarachchi, V. W. Or, Y. Lan, C. K. Madawala, E. S. Hasenecz, D. R. Crocker, C. K. Morris, H. D. Lee, K. J. Mayer, J. S. Sauer, C. Lee, G. Dorce, F. Malfatti, E. A. Stone, C. D. Cappa, V. H. Grassian, K. A. Prather and A. V. Tivanski, Size-Dependent Morphology, Composition, Phase State, and Water Uptake of Nascent Submicrometer Sea Spray Aerosols during a Phytoplankton Bloom, *ACS Earth Space Chem.*, 2022, **6**(1), 116–130, DOI: **10.1021/acsearthspacechem.1c00306**.

49 H. D. Lee, C. P. Kaluarachchi, E. S. Hasenecz, J. Z. Zhu, E. Popa, E. A. Stone and A. V. Tivanski, Effect of dry or wet substrate deposition on the organic volume fraction of core-shell aerosol particles, *Atmos. Meas. Tech.*, 2019, **12**(3), 2033–2042, DOI: **10.5194/amt-12-2033-2019**.

50 H. D. Lee, H. S. Morris, O. Laskina, C. M. Sultana, C. Lee, T. Jayarathne, J. L. Cox, X. F. Wang, E. S. Hasenecz, P. J. DeMott, T. H. Bertram, C. D. Cappa, E. A. Stone, K. A. Prather, V. H. Grassian and A. V. Tivanski, Organic Enrichment, Physical Phase State, and Surface Tension Depression of Nascent Core-Shell Sea Spray Aerosols during Two Phytoplankton Blooms, *ACS Earth Space Chem.*, 2020, **4**(4), 650–660, DOI: **10.1021/acsearthspacechem.0c00153**.

51 H. D. Lee, K. K. Ray and A. V. Tivanski, Solid, Semisolid, and Liquid Phase States of Individual Submicrometer Particles Directly Probed Using Atomic Force Microscopy, *Anal. Chem.*, 2017, **89**(23), 12720–12726, DOI: **10.1021/acs.analchem.7b02755**.

52 K. K. Ray, H. D. Lee, M. A. Gutierrez, F. J. Chang and A. V. Tivanski, Correlating 3D Morphology, Phase State, and Viscoelastic Properties of Individual Substrate-Deposited Particles, *Anal. Chem.*, 2019, **91**(12), 7621–7630, DOI: **10.1021/acs.analchem.9b00333**.

53 H. D. Lee, S. Wigley, C. Lee, V. W. Or, E. S. Hasenecz, E. A. Stone, V. H. Grassian, K. A. Prather and A. V. Tivanski, Physicochemical Mixing State of Sea Spray Aerosols: Morphologies Exhibit Size Dependence, *ACS Earth Space Chem.*, 2020, **4**(9), 1604–1611, DOI: **10.1021/acsearthspacechem.0c00153**.

54 A. Gupta and J. B. Rawlings, Comparison of parameter estimation methods in stochastic chemical kinetic models: Examples in systems biology, *AIChE J.*, 2014, **60**(4), 1253–1268, DOI: **10.1002/aic.14409**.

55 D. van Ravenzwaaij, P. Cassey and S. D. Brown, A simple introduction to Markov Chain Monte–Carlo sampling, *Psychon. Bull. Rev.*, 2018, **25**(1), 143–154, DOI: **10.3758/s13423-016-1015-8**.

56 C. S. McCluskey, T. C. J. Hill, R. S. Humphries, A. M. Rauker, S. Moreau, P. G. Strutton, S. D. Chambers, A. G. Williams, I. McRobert, J. Ward, M. D. Keywood, J. Harnwell,

W. Ponsonby, Z. M. Loh, P. B. Krummel, A. Protat, S. M. Kreidenweis and P. J. DeMott, Observations of ice nucleating particles over Southern Ocean waters, *Geophys. Res. Lett.*, 2018, **45**, 11989–11997, DOI: **10.1029/2018GL079981**.

57 R. E. Cochran, O. Laskina, J. V. Trueblood, A. D. Estillore, H. S. Morris, T. Jayarathne, C. M. Sultana, C. Lee, P. Lin, J. Laskin, A. Laskin, J. A. Dowling, Z. Qin, C. D. Cappa, T. H. Bertram, A. V. Tivanski, E. A. Stone, K. A. Prather and V. H. Grassian, Molecular Diversity of Sea Spray Aerosol Particles: Impact of Ocean Biology on Particle Composition and Hygroscopicity, *Chem*, 2017, **2**(5), 655–667, DOI: **10.1016/j.chempr.2017.03.007**.

58 L. E. Mael, G. Peiker, H. L. Busse and V. H. Grassian, Low Temperature Water Uptake of Individual Marine and Biologically Relevant Atmospheric Particles Using Micro-Raman Spectroscopy, *J. Phys. Chem. A*, 2021, **125**, 9691–9699, DOI: **10.1021/acs.jpca.1c08037**.

59 R. Patnaude, R. J. Perkins, S. M. Kreidenweis and P. J. DeMott, Is ice formation by sea spray particles at cirrus temperatures controlled by crystalline salts?, *ACS Earth Space Chem.*, 2021, **5**(9), 2196–2211, DOI: **10.1021/acsearthspacechem.1c00228**.

60 C. Deng, S. Brooks, G. Vidaurre and D. C. O. Thornton, Using Raman Microspectroscopy to Determine Chemical Composition and Mixing State of Airborne Marine Aerosols over the Pacific Ocean, *Aerosol Sci. Technol.*, 2014, **48**(2), 193–206, DOI: **10.1080/02786826.2013.867297**.

61 G. P. Schill, P. J. DeMott, E. W. Emerson, A. M. C. Rauker, J. K. Kodros, K. J. Suski, T. C. J. Hill, E. J. T. Levin, J. R. Pierce, D. K. Farmer and S. M. Kreidenweis, The contribution of black carbon to global ice nucleating particle concentrations relevant to mixed-phase clouds, *Proc. Natl. Acad. Sci. U. S. A.*, 2020, **117**(37), 22705–22711, DOI: **10.1073/pnas.2001674117**.

62 L. E. Mael, *Micro-Raman Spectroscopy as a Probe of the Composition, Ice Nucleation, and Low Temperature Water Uptake of Individual Substrate Deposited Aerosol Particles*, PhD dissertation, University of California, San Diego, 2021, **http://dissertations.umi.com/ucsd:20880**.

63 E. Attard, H. Yang, A. M. Delort, P. Amato, U. Pöschl, C. Glaux, T. Koop and C. E. Morris, *Atmos. Chem. Phys.*, 2012, **12**(22), 10667–10677, DOI: **10.5194/acp-12-10667-2012**.

64 G. Bar, Y. Thomann, R. Brandsch, H. J. Cantow and M.-H. Whangbo, On the factors affecting the contrast of height and phase images in tapping mode atomic force microscopy. Study of Phase-Separated Polymer Blends of Poly(ethene-co-styrene) and Poly(2,6-dimethyl-1,4-phenylene oxide), *Langmuir*, 1997, **13**(14), 3807–3812, DOI: **10.1021/la970091m**.

65 D. Q. Pham, R. O'Brien, M. Fraund, D. Bonanno, O. Laskina, C. Beall, K. A. Moore, S. Forestieri, X. F. Wang, C. Lee, C. Sultana, V. H. Grassian, C. D. Cappa, K. A. Prather and R. C. Moffet, Biological Impacts on Carbon Speciation and Morphology of Sea Spray Aerosol, *ACS Earth Space Chem.*, 2017, **1**(9), 551–561, DOI: **10.1021/acsearthspacechem.7b00069**.

66 M. M. Chim, C. T. Cheng, J. F. Davies, T. Berkemeier, M. Shiraiwa, A. Zuend and M. N. Chan, Compositional evolution of particle-phase reaction products and water in the heterogeneous OH oxidation of model aqueous organic aerosols, *Atmos. Chem. Phys.*, 2017, **17**(23), 14415–14431, DOI: **10.5194/acp-17-14415-2017**.

67 C. P. Kaluarachchi, V. W. Or, Y. Lan, E. S. Hasenecz, D. Kim, C. K. Madawala, G. P. Dorcé, K. J. Mayer, J. S. Sauer, C. Lee, C. D. Cappa, T. H. Bertram, E. A. Stone, K. A. Prather, V. H. Grassian and A. V. Tivanski, Effects of Atmospheric Aging Processes on Nascent Sea Spray Aerosol Physicochemical Properties, *ACS Earth Space Chem.*, 2022, **6**(11), 2732–2744, DOI: **10.1021/acsearthspacechem.2c00258**.

68 A. Welti, E. K. Bigg, P. J. DeMott, X. Gong, M. Hartmann, M. Harvey, S. Henning, P. Herenz, T. C. J. Hill, B. Hornblow, C. Leck, M. Löffler, C. S. McCluskey, A. M. Rauker, J. Schmale, C. Tatzelt, M. van Pinxteren and F. Stratmann, Ship-based measurements of ice nuclei concentrations over the Arctic, Atlantic, Pacific and Southern oceans, *Atmos. Chem. Phys.*, 2020, **20**, 15191–15206, DOI: **10.5194/acp-20-15191-2020**.